The Thesis Committee for Gavin Ray Packard
Certifies that this is the approved version of the following thesis:

Experimentally Determined External Heat Transfer Coefficient of a Turbine Airfoil Design at Varying Incidence Angles

APPROVED BY

SUPERVISING COMMITTEE:

Supervisor:

David G. Bogard

Mathew J. Hall

Experimentally Determined External Heat Transfer Coefficient of a Turbine Airfoil Design at Varying Incidence Angles

by

Gavin Ray Packard, B.S.M.E.

Thesis

Presented to the Faculty of the Graduate School of

The University of Texas at Austin

in Partial Fulfillment

of the Requirements

for the Degree of

Master of Science in Engineering

The University of Texas at Austin

May 2015

Dedication

To the pursuit of knowledge - may it always keep me gainfully employed in a competitive market

Acknowledgements

I would like to thank Dr. Bogard for his tireless efforts to teach me how to be an engineer; I like to think a little stuck in the end. Thanks to everyone at the TTCRL, Adam, Brad, Chris, Ellen, Emily, Gary, Jennifer, John, Josh, Khanh, Kyle, Noah, Robbie, and especially Sean, for creating a work environment that provided challenging and entertaining experiences over the years. Oh, and Taco Tuesdays.

Special thanks to my parents for making me. It was nearly 30 years in the works, but I might finally be an adult.

Abstract

Experimentally Determined External Heat Transfer Coefficient of a Turbine Airfoil Design at Varying Incidence Angles

Gavin Ray Packard, M.S.E.

The University of Texas at Austin, 2015

Supervisor: David G. Bogard

Predicting and measuring external heat transfer coefficients of hot gas path turbine components are important tools for gas turbine designers. Inlet temperatures often exceed the melting temperature of the materials used in such components, requiring protective measures such as thermal barrier coatings or film-cooling to prevent component failure. The external heat transfer coefficients can be used to design for the thermal loading that will ultimately lead to such failures. Modern engine designers use computational codes to predict the conditions of the hot gas components during engine operation. Before these codes can be relied upon as accurate, they must first be verified with experimental measurements. However, measuring the heat transfer coefficients can be a difficult process, especially on an actual engine component, due to the extreme temperatures and inaccessibility. As such, low speed, low temperature wind tunnels are often used to simulate a scaled version of turbine components to collect experimental data to assist in validating computational codes. This thesis details the construction of scaled up turbine airfoils to collect such data. It also provides data covering the

generation of turbulence using an array of vertical rods upstream of a linear cascade in a low speed wind tunnel at off-normal incidence flow angles.

Table of Contents

List of Tables

List of Figures

Nomenclature

SYMBOLS

A	Area
C	Chord length of the model vane
h	Convective heat transfer coefficient
H	Height of model airfoil
I	Current
P	Pitch of linear cascade
q	Heat flux
Re	Reynolds number
s	Streamwise coordinate from geometric leading edge (leading edge s = 0)
T	Temperature
Tu	Turbulence intensity
V	Voltage
y	Pitchwise coordinate of test section (geometric leading edge of center airfoil y=0)
z	Spanwise coordinate of model airfoil (bottom of airfoil model z= 0)

GREEK

β	Incidence angle
δ	Uncertainty
ε	Emissivity
ρ	Density
η	Efficiency
σ	Stefan-Boltzmann Constant
λ_f	Integral Length Scale
τ_{int}	Integral Time Scale

1. Introduction

1.1. BRAYTON CYCLE, GAS TURBINES, AND FILM COOLING

Gas turbines are a ubiquitous feature in modern day power generation and aviation. Prior to their introduction, steam turbines were the source of electrical power generation, utilizing heat to make steam in a boiler that was fed into a turbine to produce electricity. This process is referred to as a Rankine Cycle. Gas turbines differ from their predecessors by using a gas as the working fluid, typically air. This is referred to as a Brayton Cycle.

Most Brayton Cycles operate on an "open loop," meaning that the gas that is used during the process is taken in to the cycle and then exhausted at the end, meaning no recirculation of the gas takes place. This is common in both aviation and power plants, though it may seem less intuitive for the latter. With power plants, the exhaust from the turbine is still very hot, meaning it can still be used, and more and more often it is recycled, to power steam turbines. This is called a combined cycle power plant, which is quickly becoming the industry standard as their overall efficiencies can be higher than a power plant that only uses a gas turbine. A diagram of an "open loop" Brayton Cycle is shown in Figure 1.1.

In an open Brayton cycle, the compressor intakes the working gas, compresses it and feeds it into a combustion chamber where a fuel is introduced and burned. Typically, the compressor is also powered by the turbine. The combustion chamber is used to further increase the available energy of the gas before it is fed into the turbine. The turbine's function is to capture energy from the gas as it expands through the turbine, effectively converting the pressure to useful work. In a power plant turbine, this work is then used to produce electricity, and in aviation it is used to generate thrust. These steps

are summarized in Figure 1.2, with the last step being optional depending on whether to the cycle is open or closed.
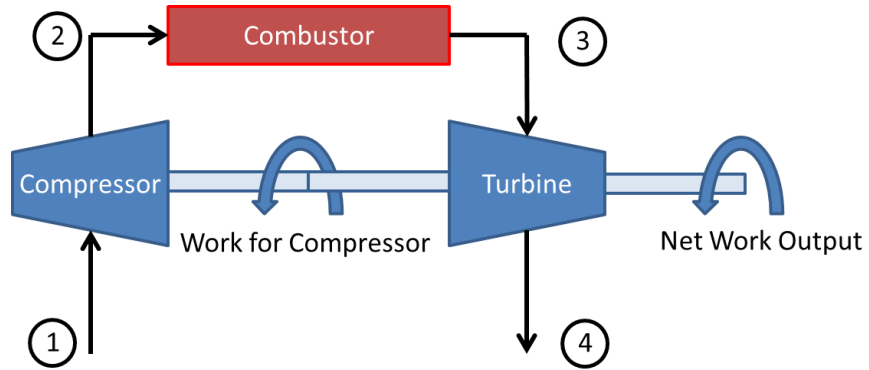
Figure 1.1: Example of Open Brayton Cycle
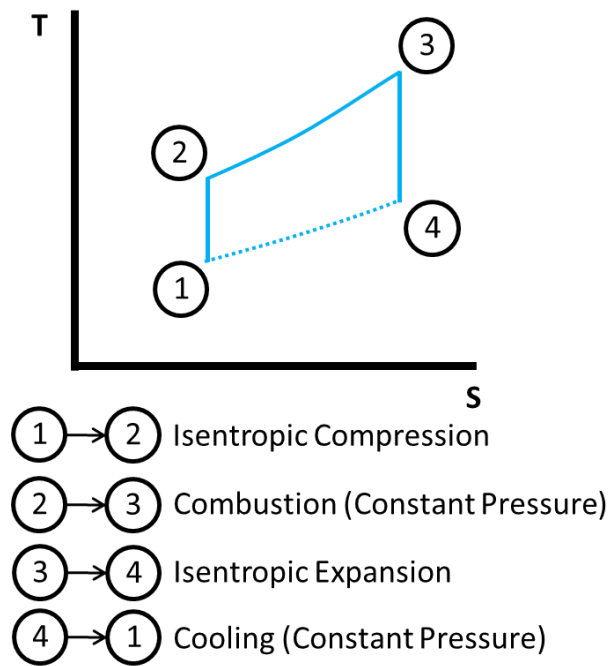
Figure 1.2: Stages of Brayton Cycle on Temperature-Entropy Diagram

The cycle illustrated in Figure 1.2 is an idealized cycle, but can still provide insight to the important variables that determine the efficiency of the cycle. Using the first and second laws of thermodynamics, one can arrive at the following equation for the efficiency of the Brayton Cycle [1]:

Equation 1.1:
$$\eta = 1 - \frac{T_4 - T_1}{T_3 - T_2} = 1 - \left(\frac{P_1}{P_2}\right)^{\frac{\gamma-1}{\gamma}}$$

where γ is the ratio of constant pressure specific heat to constant volume specific heat, or heat capacity ratio, of the gas in the cycle. From Equation 1.1 it becomes apparent that the important factors for increasing efficiency are the pressure across the compressor (i.e. going from stage 1 to stage 2 in Figure 1.1 and Figure 1.2), which also leads to indirect increase in temperature exiting the combustor, or by directly increasing the temperature exiting the combustor, T_3. The combustion process is used to raise the temperature of the gas, T_3, which leads to high temperatures entering the turbine. The pressure in the combustor does not necessarily increase, and is considered an isobaric process, as the combustor is an open container that allows the gas to flow out and into the turbine as it is heated. This heating of the gas becomes the limiting factor in turbine design.

Most gas turbines are limited by the temperature at the exit of the combustion stage. This constraint is set by the material limitations of the engine components downstream of the combustor, as continuous exposure to high temperatures can greatly impact the durability of these parts. There are several methods available to increase the temperature limitations of the parts, specifically the turbine blades and vanes, such as using nickel-based super alloys with very high melting temperatures, using a thermal

3

barrier coating (TBC) on the outside of the components, internal cooling channels, and film-cooling schemes on the airfoils. New materials, such as ceramic matrix composites (CMC's) are also being investigated for use in gas turbines[2].

Film cooling techniques rely on bleeding some of the working fluid from the compressor stage(s) and flowing it through small channels inside the turbine airfoils, turbine vanes, or end walls (three of the critical components in a turbine's hot gas path) and out through holes on the surface. This creates a thin film of "cool" gas that insulates the component from the much hotter gas that is exiting the combustor.

Over the years, the temperature of the hot gas path inlet to the turbine has increased, shown in Figure 1.3. Typical turbines today run at temperatures that far exceed the melting point of the materials used. This increase has led to increases in turbine efficiency which in turn saves on fuel costs to power the turbines. However, it is only with a combination of all the different technologies available that the temperature limit, and efficiency, can be increased.

As engine designers work to create new turbine designs, they must take into account the thermal loading that any components might encounter during the engine's operational life. Once this thermal loading is understood, design decisions such as material use, TBC necessity, and film cooling configurations can be determined.

With the modern age of computing, it is more and more likely that the designer will rely upon a computational fluid dynamics (CFD) solver to determine the aerodynamic and heat transfer conditions under which the components will operate.
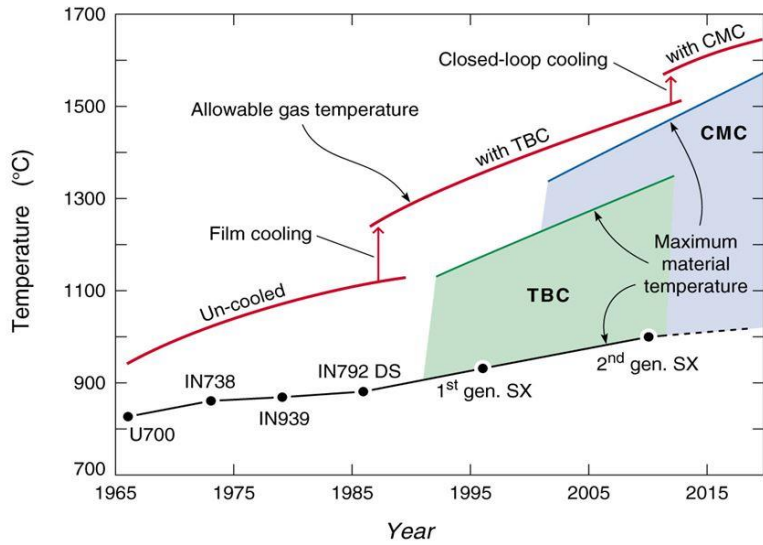
Figure 1.3: Turbine Inlet Temperatures versus Year – Source: Wadley Research Group[2]

CFD codes have improved alongside the increases in computing power that is commercially available. However, the heat transfer models continue to lag behind the aerodynamic models due to the added complexity of the solutions. For this reason, it is still very important to validate CFD codes used as a design tool prior to relying upon them. The focus of this thesis was to obtain external heat transfer coefficients for a turbine airfoil design to allow for such a validation.

1.2. EXTERNAL HEAT TRANSFER COEFFICIENT

The goal of this thesis was to measure external heat transfer coefficients for a turbine airfoil design to support validation of CFD heat transfer predictions. Two variables were changed during testing in hopes of capturing the effect of such change: incidence angle, β, and turbulence intensity, Tu. These effects, especially incidence angle, suffer from a lack of available literature. As such, this information will be useful

5

for design teams, specifically the team that has developed the geometry tested in this thesis, as they continue to develop new engines.

1.2.1. Incidence Angle

The experimental design used for this testing allowed for a change in incidence angle to be tested. Most turbine airfoils are designed to operate at a nominal angle of attack, or incidence angle. However, turbine airfoils can experience different operating conditions that can result in different incidence angles. As such, it is important for the turbine airfoil to be designed around these potential changes to reduce wear on the parts due to excessive thermal loading.

Incidence angles are typically defined relative to the axial line of the wind tunnel which is not necessarily the nominal incidence angle for an airfoil. Figure 1.4 shows the definition of incidence angle and surface location, S, used in this thesis. $S < 0$ was defined as the pressure side of the airfoil, and $S > 0$ was defined as the suction side of the airfoil and $\beta = 0°$ corresponded to the axial direction of the wind tunnel without any turning vanes.
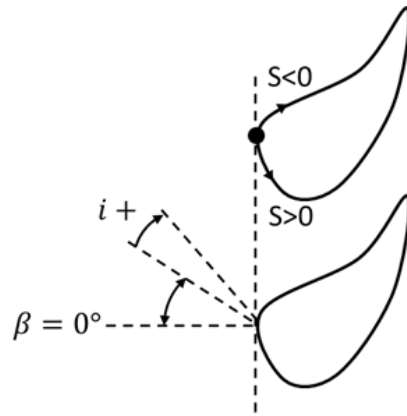
Figure 1.4: Definition of Incidence Angle and Surface Location

6

Past research has been conducted on different geometries to determine the effect of incidence angle on heat transfer coefficient. One of the predominant measurement techniques used for experimental measurements of heat transfer coefficients employs thin film probes or liquid crystal coatings to measure transient surface temperature responses to calculate heat flux and heat transfer coefficients. Thin film probes are typically placed in discrete locations along the mid-span of the airfoil, whereas liquid crystal coatings are used to coat the entire airfoil, resulting in a 3-dimensional measurement. Thin film probes operate on electrical outputs which can be measured, while liquid crystal coatings change color to indicate a temperature which is then imaged, but both measure a time dependent surface temperature.

Giel et al. [3], using a liquid crystal measurement technique, showed that a positive shift (+5°) in incidence angle from nominal resulted in a turbulent transition on the suction surface ($S > 0$) closer to the stagnation line, which is typically located near the leading edge of the airfoil. They also showed the opposite held true in that a negative incidence (−5°) from nominal delayed the turbulent transition on the suction surface, shifting it further downstream. A small effect on the location of stagnation lines and peak heat transfer coefficient were also noted.

The effects on transition location were also documented by Camci and Arts [4]. Their testing was done at nominal, +10°, +15°, and −10° using discrete thin film probes. Their results also showed a shift in stagnation point toward the pressure side as the incidence angle was increased in the positive direction while the transition of the boundary layer from laminar to turbulent on the suction surface was shifted such that it occurred earlier. These results agree with those presented by Giel et al. and were also supported by results presented by Arts et al.[5].

The location of the boundary layer transition from laminar to turbulent is an important flow feature that will affect airfoil design, as a turbulent boundary layer will result in a much higher heat transfer coefficient. A higher heat transfer coefficient will lead to a larger local thermal loading of the airfoil surface.

1.2.2. Turbulence Effect

Understanding the sensitivity of a turbine airfoil's thermal loading due to changes in turbulence intensity is a critical aspect of design. Turbines are often designed to operate at specific conditions, but it is very difficult to accurately predict the turbulence intensity that any given component will be experiencing during operation. This is due to the complexity of the flow fields exiting the combustion chamber, which are dynamic and non-uniform. As such, components must be able to withstand a range of conditions, requiring knowledge of the sensitivity to such variations in turbulence intensity. This sensitivity is often modeled using CFD, which must also be validated.

Past literature has shown that increasing freestream turbulence intensity tends to increase the overall external heat transfer coefficient along the surface of an airfoil, with the largest augmentations occurring when the boundary layer transition from laminar to turbulent flow was stimulated

. Carullo et al. [6] showed that with increasing turbulence intensity, from 2% to 12% Tu, the suction and pressure surface heat transfer coefficients of the tested airfoil increased by ~30%, with large a jump of ~80% on the pressure side and ~230% on the suction side. The large jump in augmentation on the pressure and suction sides of their results are due to an earlier transition from laminar to turbulent flow induced by a higher mainstream turbulence intensity. Their measurements also indicated that the augmentation in h was unchanged when the mainstream turbulence intensity was

increased from 12% to 14% Tu. The peak heat transfer coefficient occurred at the stagnation region.

Another study by Consigny and Richards [7] looked at the effect of mainstream turbulence on a turbine rotor blade. Their study included a low turbulence regime of 0.8% and a maximum freestream turbulence of 5.2%, which is very close to the measurements made for this thesis. Their use of a lower mainstream turbulence intensity with the nominal incidence angle led to lower increases in h, with ~15% increase around the leading edge region, and ~5% increase on the pressure and suction sides. Consigny and Richards did also measure large augmentations on the order of ~200% where earlier transition was stimulated on the suction surface. This data tends to agree with the results of Carullo et al. Again, their peak heat transfer coefficients were at the stagnation region.

Work done by Dees[8] on the C3X vane showed an increase in heat transfer coefficient corresponding to an increase in mainstream turbulence intensity shift of 0.6% to 20% Tu, that agreed with results for the same C3X vane by Ames[9] at mainstream turbulence intensities made at 12% Tu. Contrary to the work already discussed, Dees and Ames did not measure a transition to turbulence on the pressure side, but did measure one on the suction side. Overall, Dees measured a $40 - 50\%$ increase in h on the stagnation region, $30 - 40\%$ increase in h on the pressure side, and a 65% increase in h around the transition on the suction side. They showed a double peak of heat transfer coefficient around the stagnation region, but the overall peak was measured downstream on the suction side following the boundary layer transition.

Arts et al.[5] measured an increase of the heat transfer coefficient of ~7% on the pressure side due to an increase in mainstream turbulence intensity from 0.8% to 4% Tu. Arts et al. also measured a ~20% increase in h at the stagnation point and a suction side

augmentation up to ~300%. Again, this large augmentation in h on the suction side is the result of an earlier transition at the higher freestream turbulence intensity. Arts et al. results also indicate a large separation region just downstream of the stagnation region on the pressure side of the RS1S rotor blade. The overall peak heat transfer coefficient was located around the stagnation region.

In summary, the overall expectation was to see an increase in heat transfer coefficient following an increase in mainstream turbulence intensity. Most cases showed a peak heat transfer coefficient at the leading edge stagnation region, with the next highest peak occurring due to transition in the boundary layer. This was typically measured downstream on the suction side, but some cases also measured transition downstream on the pressure side. Heat transfer coefficient augmentation was typically highest at or just upstream of boundary layer transition, from ~65% to ~300%. The next largest augmentation was typically measured at the stagnation region, with increases ranging from ~20% to ~50%. Pressure side augmentation was typically lower than the other regions, from ~5% to ~15%, provided there was no transition or separation measured..

1.3. TURBULENCE GENERATION

1.3.1. Background

A typical method of providing the proper test turbulence levels required for testing airfoil geometry is by using a grid array upstream of the airfoil. This effectively generates turbulence in the mainstream of the flow that will then flow downstream at some turbulence intensity. Turbulence intensity is defined as the fluctuation in the flow velocity normalized by the average velocity of the flow, as follows:

Equation 1.2:
$$Tu = \frac{u_{rms}}{U_{mean}}$$

This equation is written for the axial direction of flow, but turbulence can and does occur in three dimensions. However, the axial direction of flow is typically the one measured and reported in literature as a single wire probe is the most common sensor used. Another important measure of turbulence is the integral length scale. The integral length scale is effectively a measure of the size of the largest turbulent eddies in the flow. During the design of a turbulence generator, turbulence intensity and integral length scale are the two variables that drive the final product.

Integral length scale can be estimated, and was done so to obtain values for this thesis, as follows:

Equation 1.3:
$$\lambda_f = \tau_{int} * U_{mean}$$

Where τ_{int} is the integral time scale and U_{mean} is the average velocity at the position of the measurement. To obtain the integral time scale, used in Equation 1.3, an autocorrelation must be performed on discrete, instantaneous velocity measurements made at one spatial location.

Equation 1.4:
$$R(\tau_j) = \sum_n \frac{(u_n - \bar{u})(u_{n+j} - \bar{u})}{u_{rms}^2}$$

Equation 1.4 gives the equation for R, the autocorrelation at a spatial location where u_n is the nth instantaneous velocity, ū is the average of the velocity data measured for the autocorrelation, u_{rms}^2 is the root mean square of the fluctuation in the velocity data measured, and u_{n+j} is the instantaneous velocity measured j time steps after n. The time steps are based upon the data rate used to measure the instantaneous velocity, which is an important factor in resolving the integral time scale. For example, if a 10 KHz rate is used, a time step of 0.0001s is achieved. The autocorrelation then compares the first instantaneous velocity to each velocity measured for each time successive time step. This autocorrelation is necessarily 1 at the start time, and drops off as the time steps advance and the flow fluctuates in instantaneous velocity. To obtain the integral time scale from the autocorrelation, the autocorrelation must be integrated from the initial time to the first time where the autocorrelation is zero or a negative value. Lower data rates will result in the autocorrelation going to zero too quickly, providing an inaccurate measure of the integral time scale.

Equation 1.5: $$\tau_{int} = \int_0^{t_0} R(t)dt$$

1.3.2. Previous Work

The design of the turbulence grid, details of which can be found in section 2.4, used for this thesis, was accomplished by Noah Mosberg as part of his Master's Thesis work[10]. His work required simulating a future test section that was not yet built in order to validate a turbulence decay correlation reported by Roach[11].

Equation 1.6:
$$Tu = A \left(\frac{x}{b}\right)^{-\frac{5}{7}}$$

This correlation considers the distance a flow travels downstream from a grid, x, normalized by the rod diameter of the grid, b. It also uses an empirical coefficient A, which Roach measured to be $A = 0.8$. Mosberg confirmed that this coefficient matched well to the data he collected in his wind tunnel configuration. It is important to note that the correlation was designed specifically for flow passing normal to the grid.

Mosberg's thesis work was an attempt to determine whether the coefficient A has a functional dependence on relative incidence angle to the turbulence grid. As such, he simulated a wind tunnel capable of varying incidence angle by placing turbulence grids at off normal angles to the flow in an axial flow wind tunnel. Mosberg's results indicated that if the solidity was held constant, the coefficient was not affected by changing incidence angles. Prior to his work, there had been no previous studies of this nature available in the literature.

1.4. OBJECTIVES OF STUDY

The work performed for this thesis had two major components. The first was the design and manufacture of the model airfoils used for experimentation. The other was the experimental measurements, of which there were two primary results: validating Noah Mosberg's turbulence correlation for the wind tunnel test section used, and measuring the external heat transfer coefficients for the tested airfoil geometry.

The design and manufacture of the airfoils is detailed thoroughly in the following chapter. The overall geometry used is a proprietary design and as such, sensitive images used are distorted or masked.

The first of the experimental measurements performed was the validation of the correlation provided by Mosberg's thesis work. As there had been no previous study regarding the influence of incidence angle on turbulence grids, it was imperative to complete this work prior to experimentally measuring other aspects of the model airfoils. This work was completed by measuring the turbulence intensity and length scales in a newly constructed test section, with the goal of validating the correlation coefficient to be used in Equation 1.6.

The second experimental measurement performed was the measurement of the external heat transfer coefficients on the model airfoil. The information resulting from such measurements is important to further the computational capabilities of engine designers. The data that was collected for this thesis provides continuous heat transfer coefficient distributions on a 2-dimensional surface of the airfoil, a quality that much of the past literature lacks. The goal of the measurements was to determine the effects, if any, of turbulence intensity and incidence angle on the heat transfer coefficients for the model airfoil tested.

2. Facility, Experimental Setup, and Uncertainty Analysis

The goal of this thesis is to present the results of experimentally measured external heat transfer coefficient distributions for a turbine airfoil design. The priority for this section is to describe the facility utilized and provide an outline of the methodology used for each of the experimental tests performed. In addition, it will detail the uncertainty analysis that was employed to quantify the potential error in the measurements that will be presented in the results section. All tests were performed in a wind tunnel, also known as the rig, which was designed and built specifically for these experiments and is shown in Figure 2.1.

Figure 2.1: Image of Wind Tunnel (The Rig)

All work was performed at the Turbulence and Turbine Cooling Lab (TTCRL) at The University of Texas at Austin. The experiments were performed using a low speed,

recirculating wind tunnel designed with a linear cascade. The airfoil models used for the study were scaled up versions of a turbine airfoil design. There are four distinct models designated as Test Article's A, B, C, and D. Additionally, there were two dummy airfoil models, a full airfoil model and a 1/3 airfoil model.

2.1. TESTING REQUIREMENTS

Testing of the turbine airfoil required a substantial amount of design and manufacturing work prior to any experimental testing. The goal of this work was to match the experimental testing requirements predetermined to match engine conditions of a theoretical new engine design. These requirements were to experimentally match Reynolds number in the wind tunnel, as well as match the pressure distribution along the model turbine airfoil, to the actual engine conditions. One of the Test Articles, Test Article D, was also required to match the Biot number and ratio of internal to external heat transfer coefficients. In addition to these parameters, requirements for turbulence levels and airfoil incidence angle inside the test section were also set, all of which will be discussed in detail within this section.

2.2. WIND TUNNEL

The wind tunnel consisted of two flow loops, a mainstream flow loop that features a test section designed to house Test Article cartridges, and a secondary flow loop designed to provide coolant to specific Test Articles. The primary loop was powered by a 50 horsepower fan that could be varied by either motor speed or blade pitch. The secondary loop was powered by a 7.5 horsepower blower and fed into a heat exchanger. The heat exchanger also featured an inlet for liquid nitrogen, which was expanded inside

coils and then mixed with the air bled from the mainstream prior to being routed into the model airfoil inlet located underneath the Test Article cartridge slot.

2.2.1. Re-design

The wind tunnel was redesigned for this project by Kyle Chavez as part of his PhD work at the TTCRL. The redesign altered the upstream contraction nozzle and downstream diffuser to reduce losses within the tunnel, and added a discrete incidence angle adjustment capability to the wind tunnel by building an entirely new test section. This allowed for experimental testing across a range of angle of attacks for the Test Articles. A CAD model of the newly designed wind tunnel test section is shown in Figure 2.2.

A linear cascade, a linear row of airfoils, consisting of a center Test Article and the full and 1/3 dummy airfoil models was used to establish a repeating boundary condition within the test section. The 1 1/3 dummy airfoils were built during the design and manufacture of Test Article A and will be discussed in that section.

As shown, two stages of turning vanes were used to redirect the flow through the test section, thus changing the incidence angle at the inlet of the airfoil cascade. It is important to note that the wind tunnel was designed to reach a large range of incidence angles, but only two angles were used for the experimental testing described within this thesis, the $-25°$ and $-35°$ incidence angles. The definition of incidence angle and the curve length, S, used to non-dimensionalize the results are shown in Figure 2.3. Note that a negative S value refers to the pressure side of the airfoil, and a positive value to the suction side. An incidence angle of $\beta = 0°$ corresponds to the test section with no turning vanes installed.

17
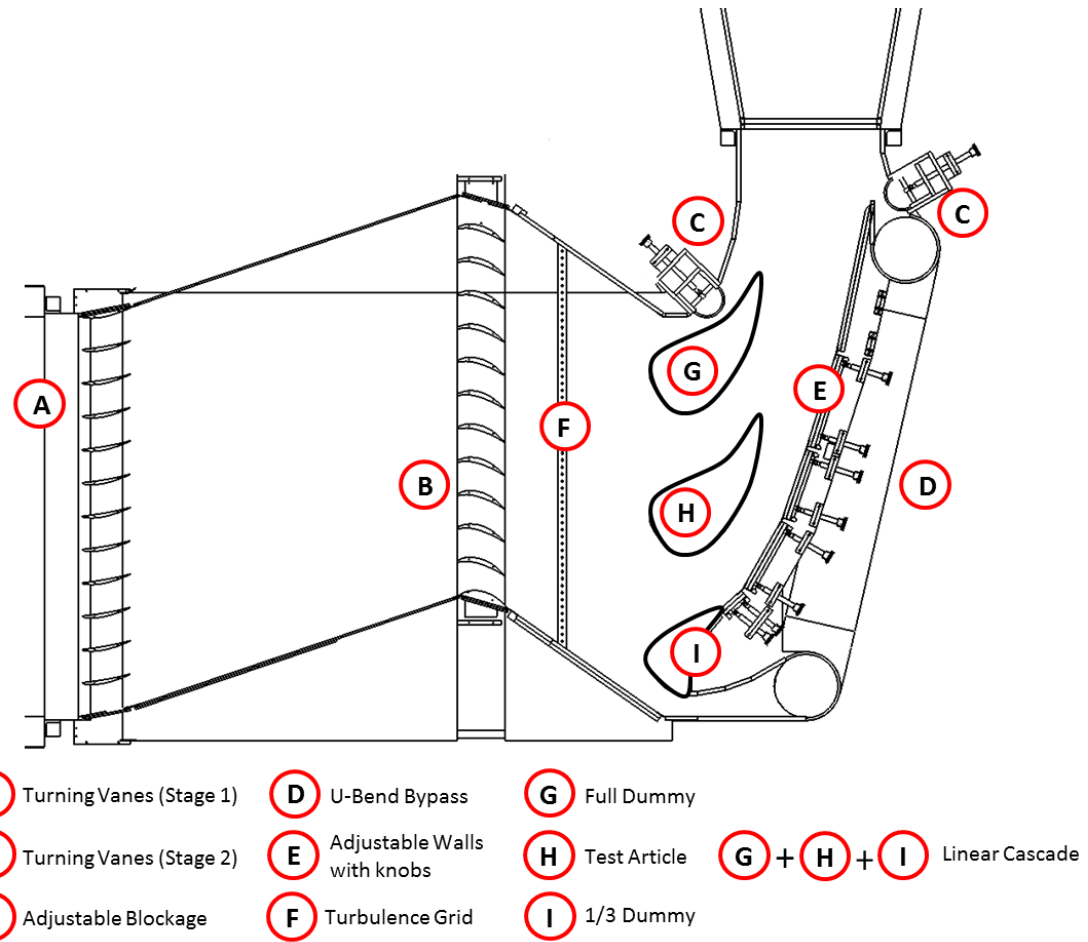
Figure 2.2: Schematic of Test Section

The angles were referenced by the amount they turn the flow relative to an otherwise axial flow through the wind tunnel with negative defined as flow turned to impact the pressure side of Test Article, illustrated below in Figure 2.4.

It is important to note that the $-25°$ and $-35°$ angles were chosen specifically as they correspond to the nominal and $-10°$ off nominal inlet angles in the actual engine. However, during the course of the project, it was discovered that an error was made and

that the nominal engine condition was actually the same as $-30°$ in the rig. This meant that the $-25°$ rig angle corresponded to $-5°$ engine angle, and $-35°$ rig angle corresponded to $+5°$ engine angle, shifting the experimental results from engine nominal and $-10°$ to $\pm5°$ of the engine's nominal inlet angle. This was once again adjusted by the flow turning by the presence of the turbulence grid. The final angles tested will be presented in the results section.
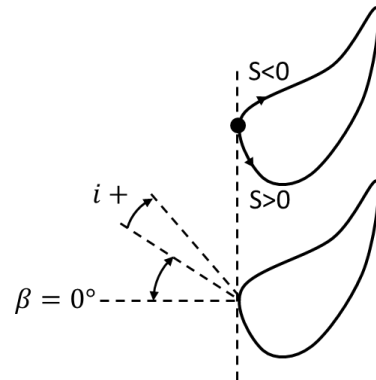
Figure 2.3: Definition of Incidence Angle and Surface Location
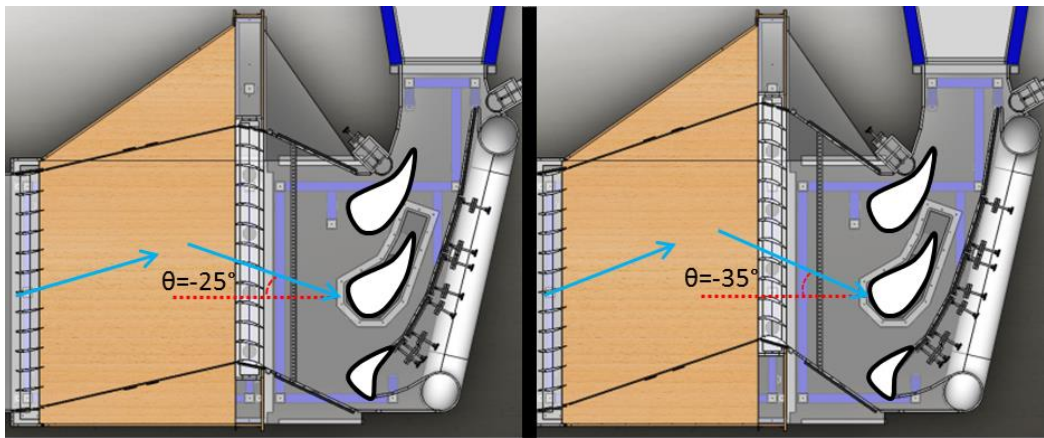
Figure 2.4: Incidence Angles Designed Towards for Testing

All data acquisition was accomplished using LabVIEW or Infra-Red (IR) Cameras. The LabVIEW VI that was utilized was created in-house specifically for the testing performed. Thermocouples and pressure transducers were connected to a computer with a 4 module National Instruments DAQ chassis. The modules used were NI-SCXI-1100 and NI-SCXI-1102 accessories and NI-SCXI-1300/1302 modules, which provided a total of 128 input voltage channels to be used for either thermocouples or pressure transducers. Measurements were performed at a rate of 833 Hz with a sample size of 4500 data points. The max data rate was based on channel limitations and the sample size was selected to minimize precision uncertainty, which is covered in more detail further on.

Four separate IR cameras were used during testing. This included FLIR brand P20, SC325, A655SC, and T620 models. All cameras were placed outside of the wind tunnel and utilized NaCl windows to view the Test Articles inside the wind tunnel during operation. The locations of these ports were determined during the wind tunnel design and will be illustrated during discussion of the heat transfer coefficient measurements.

2.3. INCIDENCE ANGLE VERIFICATION

Once the new test section was constructed, it was imperative to verify the incidence angles of the flow were to the design intent. This was done experimentally by Kyle Chavez using Particle Image Velocimetry (PIV). This process was performed upstream of the airfoil cascade in a position that allowed results unbiased by the presence of said cascade. While this was performed for all angles, only the results for the angles relevant to this thesis will be provided.

2.3.1. Design Recommendations for Future Work

Based upon interactions with the newly designed and built wind tunnel test section, there are several recommendations for future improvements. The primary improvement would be to remove the requirement of using the same parts in a mirrored configuration to achieve a similar angle. For example, the $-25°$ and $+25°$ configurations utilize the same parts but on the opposite side of the wind tunnel. This was done to reduce cost during the design phase; however, the total cost of procuring these parts would greatly improve functionality of the wind tunnel. Due to the way the parts are mounted on the wind tunnel, attempting to use one part in two different configurations requires that the mounting holes are properly aligned between the part and the two different places it is attached. As these holes are created with hand tools, the inherent inaccuracy of the process leads to misalignments, which reduces the integrity of the wind tunnel. In addition, redundant parts would suffer from less wear, prolonging the life of the wind tunnel.

The other primary change would be to reduce the number of bolts per piece to a minimum value, thereby reducing the time required to change wind tunnel configurations. Previous wind tunnel designs in the TTCRL utilized more latch and hook systems, and a retrofit for the new design would be a worthy consideration. These latches are also resistant to loosening due to vibrations during wind tunnel use.

2.4. TURBULENCE GRID

2.4.1. Turbulence Requirements

As mentioned previously, criteria were placed on the turbulence intensity and integral length scale during experimental testing. These conditions were 5% turbulence

intensity at the leading edge of the Test Article and an integral length scale of approximately 5% of the axial chord length of the Test Article. To achieve these conditions, a turbulence grid was placed upstream of the linear cascade and downstream of the second stage turning vanes. These grids consisted of vertical rods spaced uniformly across the span of the test section. An image of one such turbulence grid is shown below, in Figure 2.5.

Figure 2.5: Image of one Turbulence Grid

The vertical rods were built from aluminum rod stock, and were held in place by steel cross bars that were machined with a uniform spacing. The machining was completed using a Waterjet, as the tolerance was more than acceptable for these purposes.

The grids were designed by Noah Mosberg using his previously measured coefficient ($A = 0.8$) for the turbulence decay correlation (see introduction section). Table 2.1 lists the specifications of the turbulence grids that were used for all the turbulence measurements, as well as the heat transfer coefficient measurements.

22

The primary design restriction for these turbulence grids was to ensure that placement of the grid put it downstream of the second stage turning vanes, and far enough upstream of the linear cascade to allow for proper isotropic turbulence decay to the required $Tu = 5\%$.

The most important design criterion was to ensure that the turbulence grid would fit in the area of the test section upstream of the linear cascade and downstream of the second stage of turning vanes. This was dictated by the rod diameter, b, of the vertical rods used in the turbulence grid. However, another design consideration was the effective solidity of the turbulence grid, which was also a function of rod diameter. Typical solidity of turbulence grids is defined as follows:

Equation 2.1: $$S = \frac{b}{M}$$

Equation 2.1 defines solidity as the ratio of the rod diameter to the spacing between the rods. However, this is only applicable to flow that is normal to the turbulence grid. The grids used in this study were designed to be used with off-normal flow, and require an effective solidity, defined as follows:

Equation 2.2: $$S_\beta = \frac{b}{M * \cos(\beta)}$$

Equation 2.2 provides the definition of effective solidity that was used to design the turbulence grids used for measurements. This effective solidity was held constant for the grids to mitigate possible effects of incidence angle on the decay of the turbulence as predicted by Equation 2.3. The design process thus required selecting a rod diameter to fit

the grid within the test section limitations and a rod spacing, M, to match solidity. More detail on the design of the turbulence grid can be found in Mosberg's thesis [10].

Table 2.1: Turbulence Grid Specifications

Design rig angle (°)	0	-25	-35	$\beta > 35$
Grid Rod Diameter, b (in)	0.25	0.25	0.25	0.375
Solidity, S	0.25	0.22	0.20	
Effective Solidity, S_β	0.25	0.25	0.25	0.25

2.4.2. Turbulence Correlation

The location of this grid was determined by using the correlation discussed in the introduction, shown again in Equation 2.3, where x_f was the distance the flow will travel from the grid to the leading edge of the Test Article, and b was the diameter of the rods used in the grid.

Equation 2.3:
$$Tu\,\% = A \left(\frac{x_f}{b}\right)^{-5/7}$$

However, before this correlation could be used, the constant A was empirically determined by measuring the turbulence level at different locations downstream of the turbulence grid using a hotwire anemometer. It is important to recognize that the distance used in Equation 2.3 is the flow distance, x_f, and not the axial distance between the turbulence grid and the leading edge of the Test Article, x_a.

Equation 2.4:
$$x_f = x_a * \cos(\beta)$$

Equation 2.4 gives the geometric relationship between the axial distance and the flow distance as a function of the inlet incidence angle, β.

2.4.3. Hotwire Anemometry

The hotwire anemometer used was A.A. Lab System's AN-1003 Test Module and was paired with a single hot wire sensor 5 µm in diameter and ¼ inch wide. The hotwire probe was mounted to a traverse that could be moved parallel to the linear cascade at a known distance downstream of the grid and upstream of the linear cascade. An image illustrating the setup is provided in

2.4.4. Hotwire Measurements

The primary goal of the hotwire measurements was to validate the equation provided by the previous work of Noah Mosberg. This required testing a within the same range of x_f/b values that was available from his previous work. To accomplish this, hotwire measurements were made along the span of a single axial location 1" upstream of the leading edge of the linear cascade within the test section while the grid location was varied upstream. The effect was to provide different x_f/b locations without moving the axial location of the hotwire probe.

The secondary goal of the hotwire measurements was to provide an inlet condition to facilitate future computational work which is not reported in this thesis. These measurements were taken with the hotwire sensor placed at different axial location within the test section. In addition to the different location of the hotwire sensor, the turbulence grid was also placed into the position necessary to generate the 5% turbulence intensity at the leading edge of the airfoil model. This location was determined by using

the turbulence decay correlation, Equation 2.3, after the coefficient had been validated. The two different locations, "calibration hotwire" and "inlet hotwire" are illustrated in Figure 2.6.
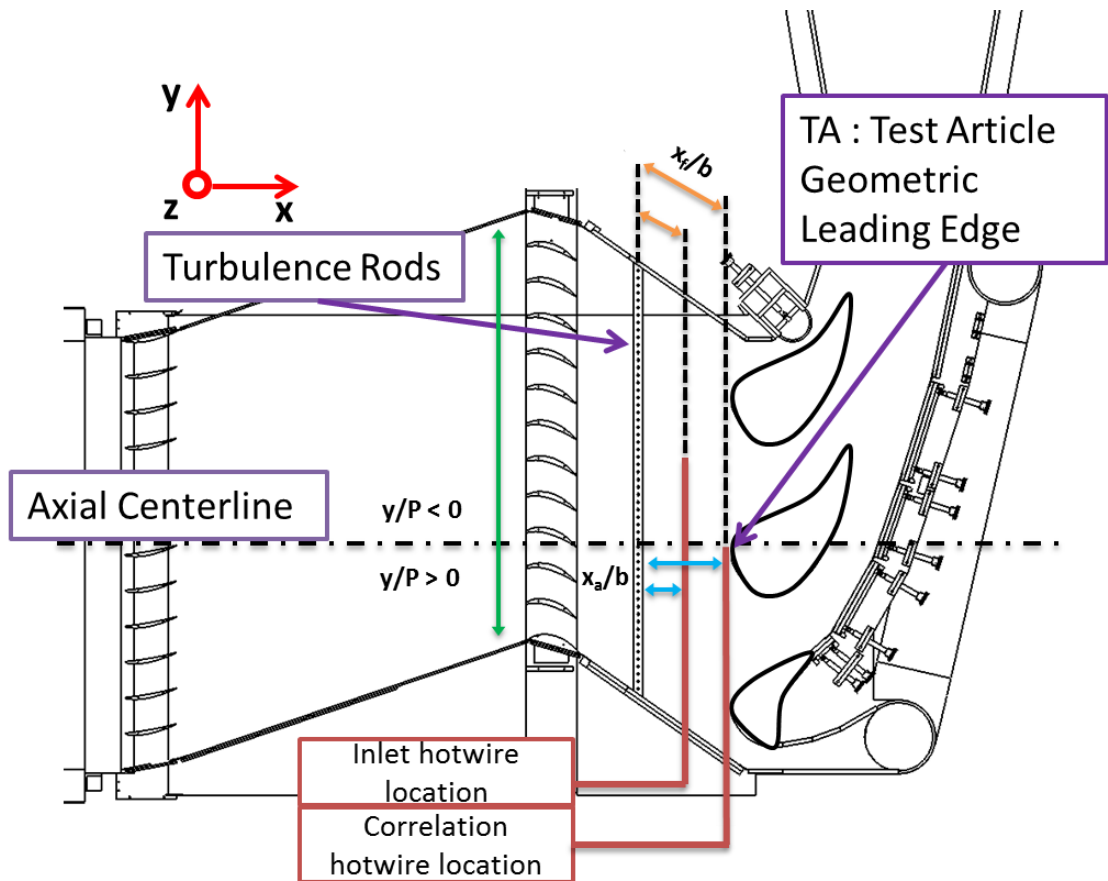
Figure 2.6: Diagram of Hotwire Testing Locations

In both hotwire cases, the hotwire sensor was first calibrated at a given point along the axial location to be traversed. Once completed, the hotwire sensor was traversed laterally to one end of the test section and data collection was initiated. At each traversed location, 100,000 samples were taken at a rate of 10 kHz and then averaged to

produce a single data point. The data rate was selected to be sufficiently high enough measure the integral length scale. A higher data rate is required to capture the changes in the instantaneous velocity necessary to generate the autocorrelation used to determine the length scale. An example plot of the autocorrelation produced using the 10 KHz sample is shown in Figure 2.7. The number of samples was selected based upon the data rate to reduce the measurement uncertainty in the fluctuation of the velocity, u_{rms}. Additionally, the 100,000 non-averaged data points were collected at periodic locations along the span for calculation of the integral length scale. This process was repeated at some locations to assist in uncertainty analysis, as described in the next section.
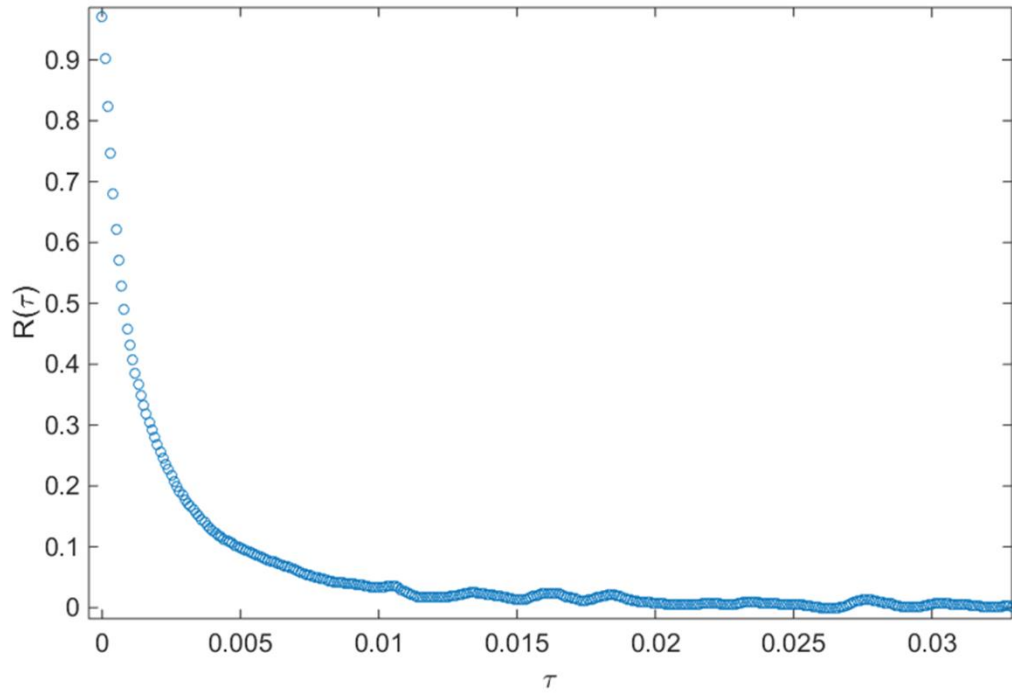
Figure 2.7: Example Autocorrelation used to estimate Integral Length Scale

The inlet hotwire testing was always completed at the required conditions for experimental testing. This includes freestream temperature and velocity with the correct

27

incident flow angle. Multiple angles were tested to determine and verify the correlation coefficient.

2.4.5. Calibration of Hotwire Anemometer

A calibration process was performed on the hotwire system prior to any turbulence measurements. To calibrate the hotwire sensor, it was placed in the wind tunnel at the "line" that was to be traversed during the measurement of data, as shown in Figure 2.6. A pitot-static tube, connected to a calibrated pressure transducer, was then placed directly above the hotwire sensor through the ceiling or sidewall of the wind tunnel to measure the same flow condition and provide a standard for calibration. The Pitot - static tube was always offset above the hot wire sensor to prevent any disturbance of the flow near the sensor.

The calibration itself was obtained by correlating calculated velocities from the pressure differential of the Pitot - static tube to the voltage readings on the hotwire anemometer. The wind tunnel's primary blower was varied to achieve range of velocities that encompassed the expected velocity range during the experimental measurements. An example calibration is shown in Figure 2.8.

The velocity, calculated from the pressure differential read with the Pitot-static tube and a pressure transducer, was plotted against the square of the voltage reading of the hotwire sensor. This resulted in a curve fit such as the one shown in Equation 2.5..

Equation 2.5: $$U = A * V^4 + B * V^2 - C$$

Once a test was completed, it was standard procedure to re-calibrate the hotwire sensor to ensure that no drift had occurred. This will be explained more thoroughly in the next section.
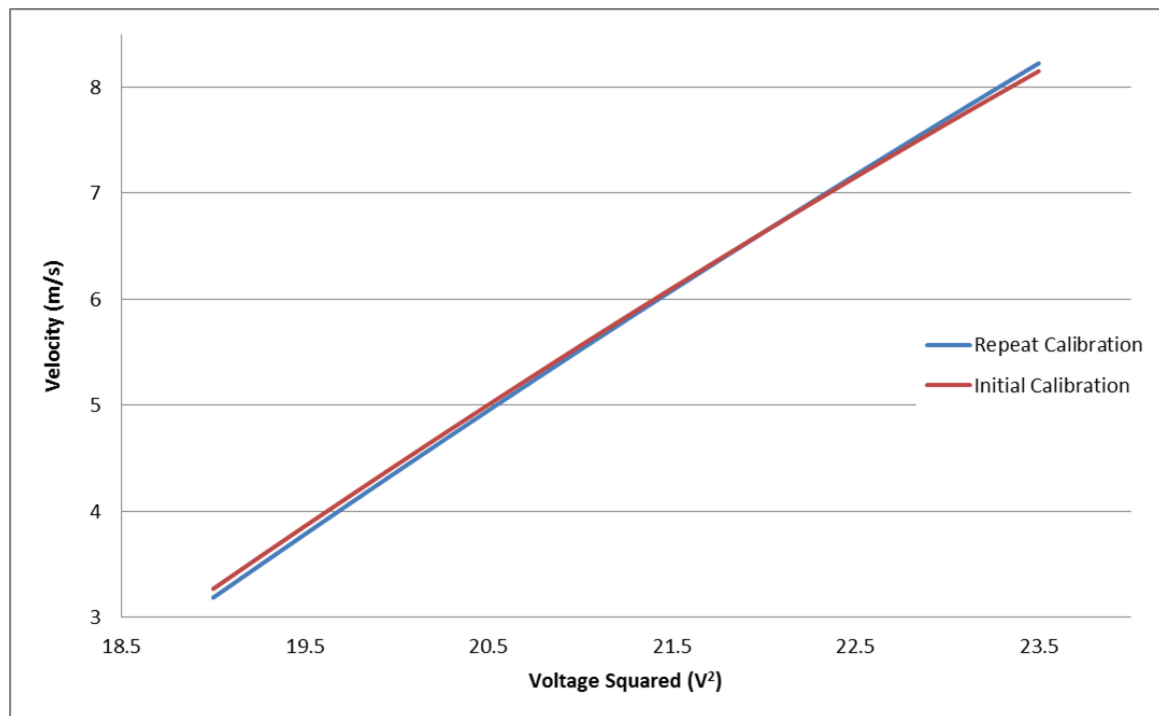
Figure 2.8: Example of Calibration for Hotwire Sensor

2.4.6. Uncertainty Analysis for Turbulence Intensity

The primary source of uncertainty was the precision of the measurement of mean and root mean square velocities. During data collection, 100,000 data points were collected at randomly selected traversed location. To then determine the precision uncertainty of the turbulence intensity, the raw 100,000 data points collected were broken into blocks of 10,000 points each. This provided 10 statistically independent samples at a given location that could be averaged together, each of which providing a statistical

average and variance that could be used to estimate the uncertainty of the measurements. Once each variance was determined, the uncertainty in each variable was calculated using the following equations:

Equation 2.6:
$$\delta \bar{u} = \frac{2\sigma_{\bar{u}}}{\sqrt{n}}$$

Equation 2.7:
$$\delta_{u_{rms}} = \frac{2\sigma_{u_{rms}}}{\sqrt{n}}$$

Equation 2.6 and Equation 2.7 also take advantage of the fact that the variance was calculated from n independent samples of data points. In all cases n was equal to 10 as the data consisted of 10 blocks of 10,000 data points. Once these uncertainties were determined, they were propagated through Equation 1.2 to determine the overall uncertainty of the turbulence intensity. This was done at each point that data was collected. The resulting uncertainties in turbulence intensity were then averaged together to generate a single uncertainty in turbulence intensity. The value listed in Table 2.2 is representative of the average turbulence intensity uncertainty for all the tests performed. The standard deviation of the average uncertainty in turbulence intensity for a given test was $\sim 0.1\%\ Tu$.

The secondary source of uncertainty of the turbulence intensity was a bias associated with the calibration process, or rather a drift in the calibration during testing. To quantify this bias, a calibration of the hotwire sensor was performed before and after each hotwire measurement test, an example of which is shown in Figure 2.8. The shown calibration is representative of the calibration drift accepted during testing. The standard error of fits for the calibrations were $\sim 0.05\ m/s$ and the average differences between

calibrations were $\sim 0.05\ m/s$. The difference in calibrations was small enough that the bias uncertainty was considered negligible.

Table 2.2: Example Uncertainty in Turbulence Intensity

Deviation / Uncertainty	Magnitude	Units
$\sigma_{\bar{u}}$	0.09	m/s
$\sigma_{u_{rms}}$	0.03	m/s
$\delta\bar{u}$	0.061	m/s
δu_{rms}	0.019	m/s
δTu	0.33%	

Uncertainty in the lengthscale was measured by taking several measurements in the same location and comparing the resulting lengthscale analysis results. This was considered the precision uncertainty in the lengthscale.

2.5. TEST ARTICLE A AND DUMMY AIRFOILS

One of the primary goals of this thesis was to experimentally measure the heat transfer coefficient distribution for the model airfoil. This required operating the wind tunnel test section in a known aerodynamic setting to facilitate future CFD validation with the obtained data. This section details the design and manufacture of the model used to set this condition, as well as the experimental setup.

2.5.1. Purpose

Test Article A and the 1 1/3 dummy airfoils were used to measure, set, and verify the pressure distribution of the Test Articles. This is an important feature of the test

section. The goal of the linear cascade is to establish a periodic flow condition on the airfoil model that is undergoing testing. Most wind tunnel test sections utilize a larger cascade of 5-10 smaller airfoil models and take measurements off the middle airfoils, assuming that the presence of several of the airfoils to either side forces a periodic condition within the cascade. However, this requires either a very large test section or a smaller airfoil model. To overcome this limitation and preserve the size of the larger airfoil models, which provides a finer resolution for IR image data, the 2 1/3 cascade method relies upon an adjustable outer wall and bypass flows through the outer passages that allow adjustment of the flow conditions to achieve periodicity. In order to determine where the walls and blockages must be set, computational fluid dynamic (CFD) simulations of the airfoil model in an infinite cascade (infinitely repeating boundary condition) were utilized to provide the expected pressure distribution around the model airfoil surface. Measurements of the pressure distribution were then made using Test Article A in real-time to assist with adjusting the outer walls and bypass flows until the pressure distribution prediction was matched.

2.5.2. Design and Manufacture

Test Article A and the 1 1/3 dummy airfoils were constructed out of General Plastic's R-3315 "Last-A-Foam," a rigid, high-density polyurethane foam. The airfoil models were first generated with SolidWorks, a computer-aided design (CAD) program. The airfoil CAD models were then used to CNC machine the foam airfoil models The foam was purchased in 24" (W) x 100" (L) x 3" (T) blocks which were machined into 3" thick cross sectional slices of the Test Article geometry. Once machined, the slices were attached to together using a polyurethane based adhesive, Gorilla Glue.

32

Test Article A's profiles were designed and machined to have hollow passages supported with internal ribs to facilitate instrumentation. Additionally, 34 small channels (0.05" wide) were cut into the top edges of 3 profile slices, 22 on the mid-span slice and 6 each on the slices above and below mid-span, as illustrated in Figure 2.9.

Each channel was then used to hold, in combination with Gorilla Glue, steel hypodermic tubing with 0.05" outer diameter (OD). The hypodermic tubing was connected to a 10' length of rubber tubing with a heat shrink seal. The rubber tubing was routed along the channels and through the top of the airfoil model, allowing connections to pressure transducers to be made outside the wind tunnel, shown in Figure 2.10. Care was taken to ensure that the breakouts of the pressure taps used to measure the pressure were flush to the outer surface of the airfoil model, an important feature of static pressure taps.
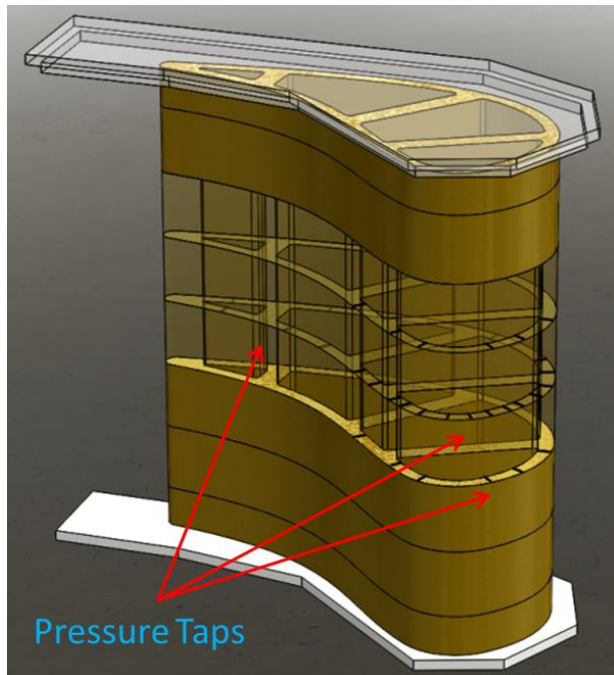
Figure 2.9: Pressure Tap Locations

The full dummy airfoil and 1/3 airfoil were also machined into 3" thick cross-sectional slices but they did not have the internal channels cut into them. All Test Articles and dummy airfoils were also fitted with top acrylic lids keyed to fit in the proper location of the wind tunnel, ensuring they fit in a repeatable manner. The Test Articles were also fitted with a bottom acrylic lid used to interface with the airfoil inlet below the wind tunnel, as shown in Figure 2.11. This cartridge design was first employed on the previous iteration of the wind tunnel, and has been proven to allow for relatively quick and easy changing of the Test Articles from one to the next.

Figure 2.10: Pressure Taps routed through Airfoil Internals

The airfoil inlet was designed as a structural support for the Test Articles, as well as an interface for the coolant loop to the Test Articles C and D, and is detailed in 2.7.2.
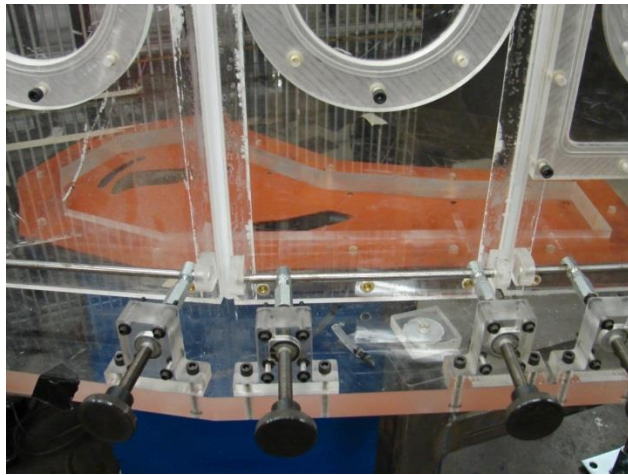
Figure 2.11: Image of Interface Slot to hold Test Articles

2.5.3. Improvements for Future Work

The dummy airfoils could be slightly improved by altering the wind tunnel floor to allow for a bottom lid to be attached. This would improve the alignment of the dummy airfoils, but ultimately, this is not a required step, as they currently perform to design intent.

2.5.4. Pressure Distribution Matching

To match the pressure distribution, adjustments to the physical geometry of the test section were made. The first adjustment is made to the outer walls of the test section that parallel the suction side of the Test Article. The other adjustment that can be made is to the blockages present on the suction side of the 1/3 dummy airfoil and the pressure side of the full dummy airfoil, which can be located on the schematic of the test section.

The pressure distribution was tracked in real time using static pressure measurements along the airfoil surface, provided by the pressure taps embedded at the mid-span and measurements from a pitot-static probe, made just downstream on the

suction side of the Test Article. The measured pressures were then used in the following equation to determine a coefficient of pressure, C_p:

Equation 2.8:
$$C_p = \frac{P_{total,outlet} - P_{static,midspan}}{P_{total,outlet} - P_{static,outlet}}$$

Measured Cp values were computed in real time using LabVIEW, with results plotted on an overlay of the CFD predicted Cp distribution. This allowed for real time adjustments to the walls and blockages to be reflected in the measurements, assisting in the process of setting the proper pressure distribution.

In conjunction with matching the CFD provided pressure distribution, the stagnation line of the Test Article and the dummy airfoils were also matched to CFD predicted values. These two criteria were used to ensure that the infinite linear cascade boundary conditions were met, a critical part of experimentally validating future CFD code.

In addition to the mid-span pressure distribution, Test Article A could also be reconfigured to measure from 18 static pressure taps with 6 located at mid-span, 6 just above mid-span, and 6 just below mid-span. These pressure taps were grouped into 3's, with each grouping aligned at the same streamwise location of the Test Article. This configuration allowed a measurement of variations in the spanwise direction of the flow field to be made. This was an important measurement to validate the design of the test section was nominally 2-dimensional, which would be confirmed by a constant pressure in the spanwise direction at any location around the airfoil model's surface.

It should be noted that initial testing to verify design intent determined that there was too much flow loss in the outer bypass loop, which begins on the suction side of the

1/3 dummy airfoil, continues through a U-shaped PVC pipe, and ejects back into the mainstream. This required the addition of an inline duct fan to overcome the losses and assist in ensuring the pressure distribution could be met. The fan used was a 12" MAXFAN purchased from CAN USA, and was installed by increasing the diameter of the existing PVC piping from 8" to 12", as shown in Figure 2.12.

Figure 2.12: Image of Bypass

2.5.5. Uncertainty in Pressure Distribution

Uncertainty in the coefficients of pressure was performed by propagating uncertainty in the pressure measurements through Equation 2.8, a method described by Moffat [12]. The sources of uncertainty in pressure measurements were split into bias and precision uncertainties.

Bias uncertainty was the result of a fossilized uncertainty present due to the calibration, example shown in Figure 2.13, of the pressure transducers used during the data collection. These transducers were calibrated against a micro manometer, and the

uncertainty of the calibration was calculated using the standard error of fit. This was considered an overestimate of the uncertainty in the measurement. In past work at the TTCRL, the bias uncertainty was dominated by the "zero-drift" of the transducers during experiments. During the experimental measurements taken for this thesis, the zero-drift of the transducers was found to be very small, on the order of $\sim 0.01\ Pa$. This fossilized uncertainty is part of all pressure measurements used throughout this thesis, but was determined for each transducer independently.

Precision uncertainty was minimized by collecting at least twenty data points, with each data point consisting of an average of 4500 pressure measurements over a 5 second period. Examples of typical values for both the precision and bias uncertainty of the pressure measurements, and their effect on the C_p measurements, are listed in Table 2.3. The uncertainty reported in the table is consistent with the pressure distribution test to test repeatability that was measured during experimentation.
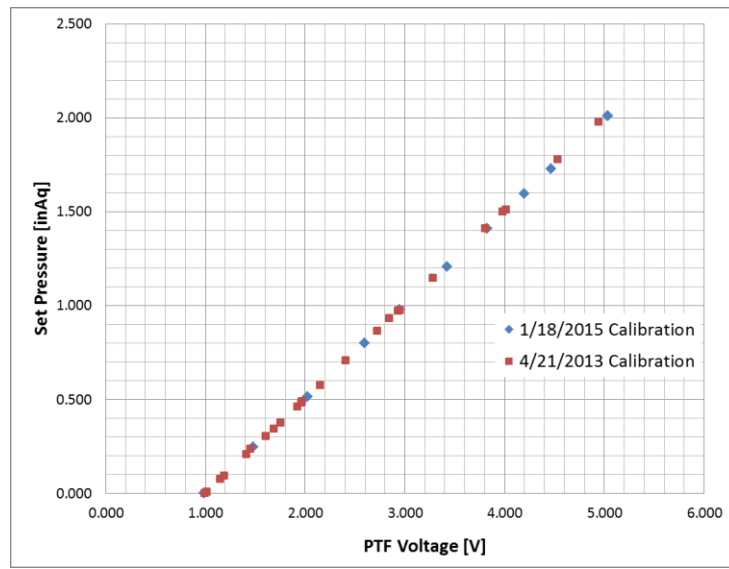
Figure 2.13: Example Calibration for Pressure Transducer

Table 2.3: Example of Uncertainty in Pressure Distribution

Source of Uncertainty	Magnitude	Units
Static Pressure Bias	1.16	Pa
Total Pressure Bias	2.16	Pa
Static Pressure Precision	0.19	Pa
Total Pressure Precision	0.04	Pa
Total Uncertainty in C_p	0.015	

2.6. TEST ARTICLE B

Test Article B was the model airfoil designed and manufactured to complete the heat transfer coefficient measurements. This section details the design and manufacture of Test Article B and the experimental setup used to obtain the final heat transfer coefficient data.

2.6.1. Purpose

The design intent for Test Article B was to provide a method of experimentally determining the external heat transfer coefficient distribution on the model airfoil. As such, the model was covered with a metal shim that provided a method of heating the surface with a constant heat flux source. This surface was then imaged with IR cameras to provide a corresponding map of the surface temperatures. This, as well as measurements of the mainstream temperature, were used to generate a map of the external heat transfer coefficients for the airfoil.

2.6.2. Design and Manufacture

The base for Test Article B was built in the same manner as Test Article A, using the same R-3315 polyurethane "Last-A-Foam." However, once the profile slices were glued together, Test Article B was returned to the machinist to cut 0.5" (W) x 12" (L) x 0.08" (T) channels near the trailing edge on both the pressure and suction sides of the airfoil, as shown in Figure 2.14.

These channels were used to house copper bars used to provide an electrical contact to steel shim that was attached to the outer surface of Test Article B. This steel shim was 12" (W) x 44" (L) x 0.002" (T) Type 301 Stainless Steel Shim Coil purchased from Trinity Brand Industries.
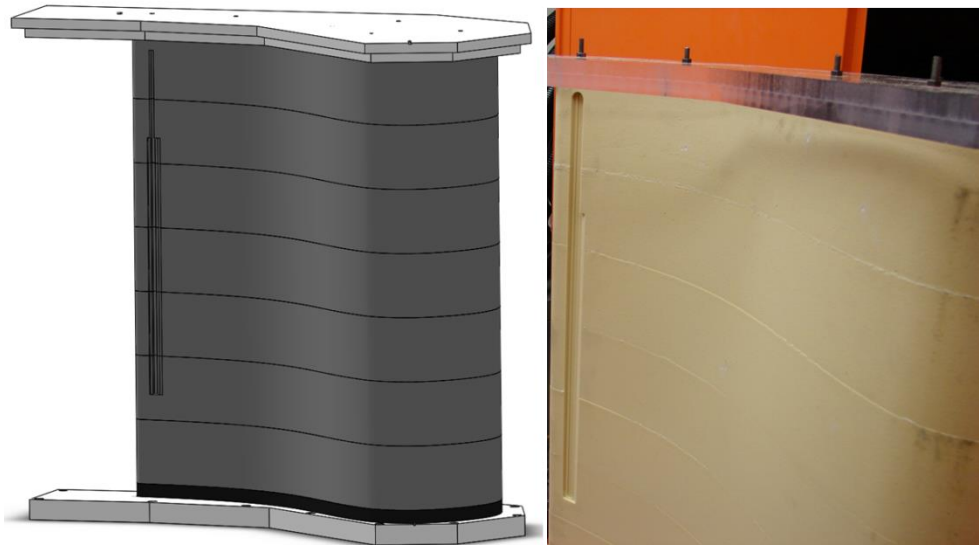

Figure 2.14: SolidWorks (left) and Actual (right) Model of Article B

Attaching the steel shim to the polyurethane surface proved challenging, but ultimately was successful. First, a 12" wide layer of VHB tape, 3M F9460PC, was used

to increase the adhesive capability of the polyurethane where the steel shim was to be attached. Secondly, double-sided tape, Scotch 410M, was placed in 12" vertical strips along the VHB tape and smoothed using a squeegee. Finally, the tape cover was removed and a thin layer of high temperature electronics epoxy, purchased from McMaster-Carr, was used to coat the outer layer of double sided tape. The steel shim was then placed into position and taped along the outer edges to hold it in place while the epoxy cured.

Copper bus bars, each of dimensions 0.25" (W) x 12" (L) x 0.0625" (T) with holes drilled along the length, were used to hold the ends of the shim and provide an electrical connection for the power supply. The top halves of the bus bars had countersunk holes, while the bottom bus bars only had through holes. The bottom half of each bus bar was used to position holes drilled into the bottom of each channel. Brass helicoils were then epoxied into the holes, and the bottom bus bars were then epoxied on top of the helicoils, taking care to align the holes with the respective helicoils. Once this epoxy was cured, the ends of the shim could be placed on to the bottom bus bar and holes made to facilitate clamping. Brass countersunk screws were used to attach the top bus bar to the bottom bus bar and hold the shim in place. A silver based conducting paste was coated to either side of the shim to be clamped prior to final attachment of the bus bars.

The final Test Article B had a constant heat flux plate made of steel shim that conformed to the curvature of the airfoil. The two ends of the shim were connected to copper bus bars that were embedded into the tail section of the airfoil such that they were flush with the surface, preventing disturbance to the flow during testing. These copper bus bars were long enough to protrude through the top lid of the Test Article, where a connection was made to a DC power supply, shown in Figure 2.15.

The Test Article and heat flux plate were both spray painted matte black with Camouflage spray paint. Fiduciary marks were made along the airfoil using silver paint pens and stencils. These began at the geometric leading edge, and proceeded in 0.25" increments along the airfoil length to the bus bars. Extra hash marks were made on every 5th inch to assist in identifying locations during post processing of data.

A final part of the construction of Test Article B was placing surface thermocouples on the internal walls. While the polyurethane foam used for the construction has very low conductivity (0.044 W/m^2-K), it still conducts heat. As such, internal thermocouples were placed along the internal walls to provide a discrete temperature map to allow for the computation of a conduction correction.

Figure 2.15: DC Power Supply (left) and Connection to Test Article B (right)

2.6.3. Improvements for Future Work

Test Article B was not easily constructed, and only through use of the model for data collection did it become apparent what could be done to improve the design for the future.

The most important improvement would be the process of attaching the steel shim. The process used can be simplified to two steps. First, use the high temperature epoxy to create a very thin coating on the area where the steel shim is to be attached. Once cured, this epoxy will provide a much better adhering surface than the polyurethane foam. The same double sided tape as used before can then be used to complete the shim attachment. It is important to continue to use tape in conjunction with the epoxy, as it has more flexibility. This becomes imperative when the heat flux plate is in operation, as the elevated temperatures will cause differing amounts of thermal expansion in the foam and the shim. With the rigidity of the epoxy, the steel shim will break off, a result that was verified by another student that was constructing a very similar Test Article.

The other major improvement to the heat flux plate would require a greater amount of planning prior to construction, but would ultimately provide a large payoff. Before testing, the IR cameras must be calibrated to a standard, typically a thermocouple on the surface of the heat flux plate. This is a difficult process to complete, as will be discussed in the results section. One way to overcome this difficulty would be to embed thermocouples on the underside of the steel shim as the heat flux plate is being constructed. These thermocouples would be permanently attached, with no danger of being broken or damaged, provided proper care is taken of the external wiring. The planning stage would require determining where each thermocouple would need to be placed to ensure that each camera views the proper number of thermocouples in the

proper positions. These positions would then require a small hole to be drilled into the foam, allowing the thermocouple wiring to be fed into the inner cavity of the airfoil model while the leads of the thermocouple would be welded to the underside of the steel shim.

If the heat flux plate is modified as described, calibrations could be conducted simultaneous to the experiment, as the embedded thermocouples would provide an active standard for the IR cameras. This would greatly reduce the time spent getting good calibrations, improve the uncertainty associated with these calibrations, reduce the post-processing time of the calibrations, and simplify the post-processing of the experimental data.

2.6.4. Heat Transfer Coefficient Experimental Design

Heat transfer coefficient measurements were completed using IR thermography and Test Article B. As the electrical power was run through the heat flux plate attached to the airfoil model, it was dissipated through resistive heating. The IR images provided a temperature map of the surface of the heat flux plate, which can be used to calculate the heat transfer coefficient at any point using Newton's Law of Cooling.

Equation 2.9: $$q''_{conv} = h(T_{surface} - T_\infty)$$

Equation 2.9 was solved for h, the heat transfer coefficient, to give Equation 2.10.

Equation 2.10: $$h = \frac{q''_{conv}}{(T_{surface} - T_\infty)}$$

All values on the right hand side of Equation 2.10 were known or measured during the experiment. The mainstream temperature, T_∞, was an average value measured

from three separate thermocouples, one just upstream of the Test Article leading edge, one in the suction side passage between the Test Article and the 1/3 dummy airfoil, and one in the pressure side passage between the Test Article and the full dummy airfoil. The Area, A, was a known value based on measurements of the heat flux plate, and the surface temperatures were measured with IR cameras. The power input by the DC power supply, q, was calculated using the following equation:

Equation 2.11: $$q_{total} = IV$$

The current, I, was measured through a shunt resister wired in-line with one lead from the power supply to one bus bar. The voltage drop, V, was measured across the heat flux plate directly using a voltmeter. The voltage measurement was made on the steel shim part of the heat flux plate, so as to get a more accurate measurement of the voltage drop in the shim and bypass the resistive heating losses along the wiring from the power supply and across the bus bars.

However, the power calculated with Equation 2.11 was not the heat flux that was used in Equation 2.10. As mentioned in the description of Test Article B's manufacture, surface thermocouples were placed along the inner walls to allow for a conduction correction. Equation 2.12 was used to calculate the amount of through-wall conductive heat flux at the locations of the internal thermocouples. These calculations were based upon discrete thermocouples inside the airfoil. A piece-wise cubic interpolation (PCHP) from one thermocouple to the next was used to generate an internal temperature map with constant temperatures measured in the spanwise direction due to the low conductivity of the material. Prior to the experimental measurements, it was expected for the internal

45

surface temperatures to remain relatively constant around the curvature of the blade. However, as shown in Figure 2.16, this was not the case. In the end, it was determined that the conductive heat flux was relatively small, $< 5\%$ of the total heat flux, and that the ΔT through the wall was also not constant. Figure 2.17 shows that the ΔT did generally follow the trend of the external surface temperature and even the increase in the internal surface temperature at $S/S_{max} = 0.18$ had no noticeable effect on the external surface temperature.
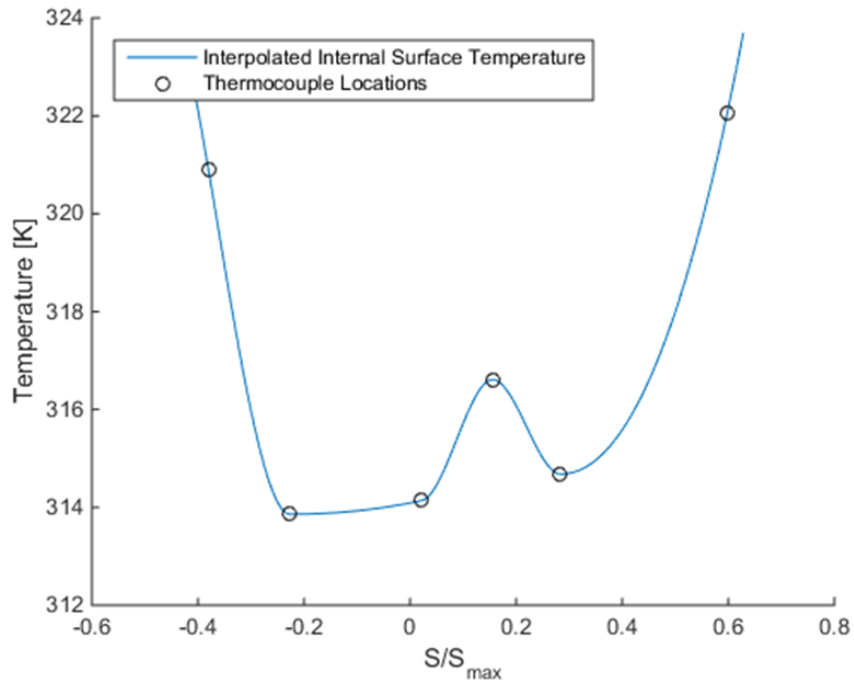
Figure 2.16: Interpolation of Internal Surface Temperatures

Equation 2.12:
$$q''_{cond} = \frac{k}{t}(T_{external,surf} - T_{internal,surf})$$

The thickness, t, was measured and the thermal conductivity, k, was known. The external surface temperature was measured with IR cameras, and the internal surface temperature with surface thermocouples. In addition to the conductive flux into the foam walls, the radiative heat flux must also be removed from the total heat flux value in order to isolate the convective heat flux needed to calculate the heat transfer coefficient.

Equation 2.13: $$q''_{rad} = \epsilon\sigma(T^4_{surface} - T^4_\infty)$$

Figure 2.17: Example of Temperature Gradients along Airfoil

47

The Stefan-Boltzmann constant, σ, was known and the emissivity, ε, for acrylic walls and for the black paint used to coat Test Article B were both specified as approximately 0.95 by manufacturers. Equation 2.13 assumed that the inside of the walls of the test section were at the same temperature of the mainstream flow and that the airfoil did not view itself. Any deviations from these assumptions were considered negligible.

Once the conductive and radiative heat fluxes were calculated, a simple energy balance on the surface of the heat flux plate yielded the following expression:
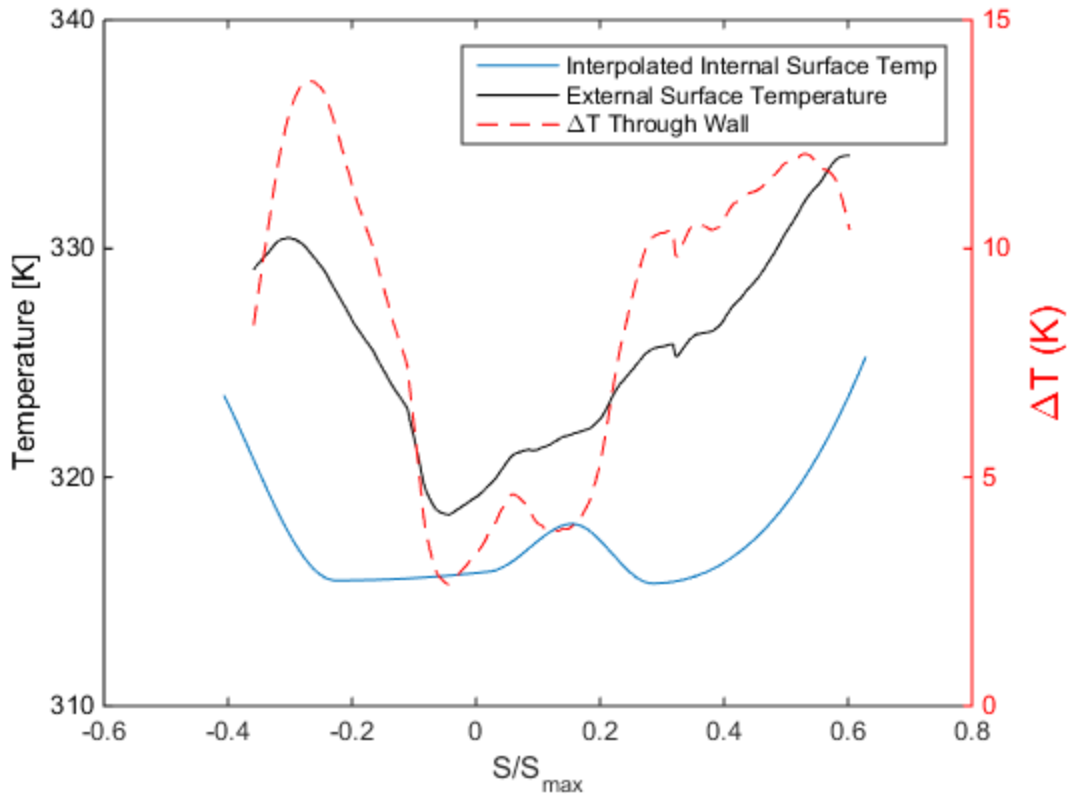
Equation 2.14: $$q''_{total} = q''_{conv} + q''_{rad} + q''_{cond}$$

Using Equation 2.10, Equation 2.11, Equation 2.12, Equation 2.13, and Equation 2.14, the heat transfer coefficient was determined:

Equation 2.15: $$h = \frac{q''_{total} - q''_{rad} - q''_{cond}}{(T_{surf} - T_\infty)}$$

2.6.5. Measurements of Heat Transfer Coefficient

Measurement of the heat transfer coefficient first required setting the pressure distribution using Test Article A. Once this was complete, the wind tunnel was turned off, Test Article A was removed, and Test Article B was inserted into the wind tunnel. The wind tunnel was then turned back on, and the mainstream temperature was allowed to reach steady state. Once this was completed, the heat flux plate was energized and also allowed to reach a steady state condition. This was determined by tracking the temperatures of internal thermocouples until they were at a nearly constant value

$(\frac{dT}{dt} \leq 0.001 \frac{K}{s})$ and generally took 30-45 minutes after energizing the heat flux plate. The temperature of the heat flux plate was set such that the minimum surface temperature provided a ΔT with the mainstream of at least $15\ K$, so as to reduce the uncertainty associated with the measurements. This typically resulted in a total heat flux of $800\ W/m2 \cdot K$.

This process worked under the assumption that the wind tunnel's pressure distribution would not be changed by the process of removing one test article and inserting another. This was verified by removing Test Article A, re-inserting it, and verifying that the pressure distribution was unchanged.

Upon reaching a steady state condition, the measurement process was then performed by taking images with IR cameras while simultaneously collecting temperature data and velocity data. Four IR cameras were used to view different yet overlapping regions of the Test Article. Figure 2.18 shows how the cameras were positioned during testing.

The cameras were individually utilized in sequence, with mainstream temperature and tunnel velocity being measured simultaneously to each image captured. Before and after each camera had been used to image the airfoil surface, the current was measured across the shunt resistor on the power supply and a port on the downstream section of the wind tunnel was opened to measure the voltage drop across the heat flux plate. The current and voltage were both found to exhibit only a negligible variation between each check.

This process was generally repeated 3-5 times per experiment to ensure in-test repeatability of the data. Each time the port just downstream of the Test Article was

removed and replaced, the tunnel was allowed to return to steady state, requiring about 10-15 minutes between data collections.
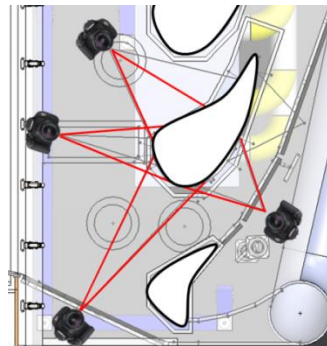
Figure 2.18: Camera Locations during Data Collection

In order to obtain temperature data from the IR cameras, the image captured (of .jpeg format) was imported into the ThermaCam program. This program was used to create a map of pixel coordinates corresponding to the fiducial marks painted onto the Test Article surface. These coordinates, along with the measured temperature and heat flux data, were then input into a MATLAB script authored by Kyle Chavez, a graduate student at the TTCRL, which would transform the images into flat, rectangular images, as well as perform the necessary calculations, as detailed in 2.6.4, to create a corresponding map of heat transfer coefficients.

2.6.6. Calibration of IR Cameras

The calibration of the IR cameras was performed by measuring the surface temperature with both the IR camera, and a calibrated thermocouple. This was accomplished by first attaching an array of calibrated surface thermocouples to the mid-span of Test Article B, shown in Figure 2.19.
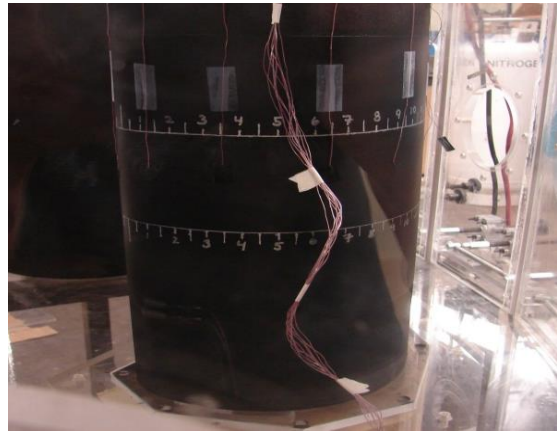
Figure 2.19: Article B prepared for IR Calibration

To attach the thermocouples, many different methods were attempted. The final process involved using a piece of double-sided scotch tape between the heat flux surface and the surface thermocouple lead. Once attached to the surface of the heat flux plate, a piece of black electrical tape was then placed on top of the thermocouple lead. Care was taken to determine the position of these thermocouples along the curvature of the airfoil such that each IR camera viewed one thermocouple that was also viewed by the adjacent camera. That is, there was always at least one thermocouple that was visible to two IR cameras. This was an important part of the setup as the IR cameras were known to have a dependency on viewing angle, with more extreme viewing angles resulting in different temperature readings from more normal views. The overlap ensured that the appropriate temperature was measured for each camera during the calibration process in order to account for the viewing angle dependency.

Once the thermocouples were attached and Test Article B was placed into the wind tunnel, the wind tunnel was set to a very low speed setting. This allowed for the mainstream temperature to be heated via the upstream heat exchanger while the

51

hydrodynamic effects around the airfoil were minimized. It was important to minimize the hydrodynamic effects to prevent a bias in the surface thermocouple readings.

After the tunnel condition was set, the heat flux plate was energized. The plate was adjusted to different levels of heat flux while the surface temperatures were monitored. These adjustments to heat flux were made until all temperatures measured during the testing were bracketed. At each set point, the heat flux plate was allowed to reach a steady state condition. Once complete, IR images were taken of the thermocouples while LabVIEW captured time-averaged temperature data from the thermocouples.

To process the IR images, ThermaCam was employed. This allowed the surface temperature of the thermocouple measured by the IR camera to be obtained. There were a number of iterations on properly attaching the surface thermocouples to the heat flux plate of Test Article B. Every variation will not be detailed, but the overall methods will be summarized. The first method was to attach the thermocouple to a small piece of steel shim with epoxy and paint the outer surface black. The steel shim was then taped to the surface of the heat flux foil using double sided scotch tape. An image of the resulting method is shown in Figure 2.20. It is apparent from this method that there is a large difference between the temperatures of the steel shim tabs compared to the surrounding regions. Furthermore, flow effects were apparent, such as streaks of higher temperatures downstream of wires and the steel shim tabs. This suggested the possibility of a bias being introduced into the calibration process for the IR cameras. As such, another method was used.
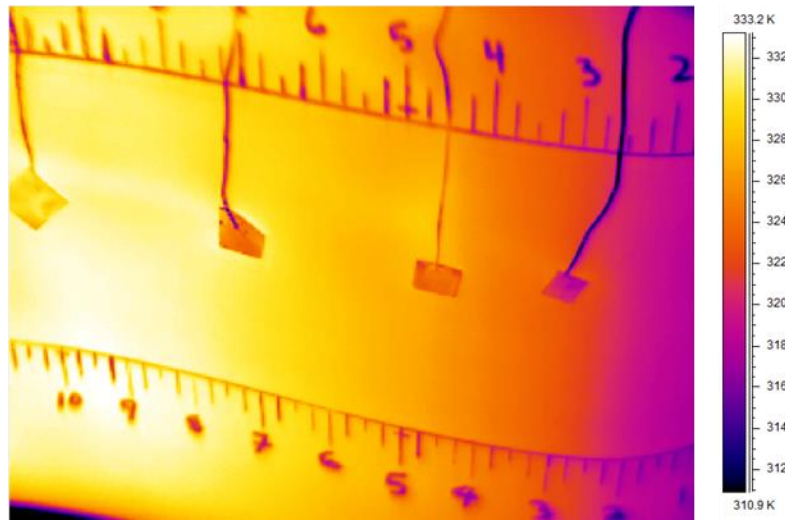
Figure 2.20: Steel Shim Tabs Method (Un-calibrated Temperatures)

The second method, and the one that provided the best results, was to attach the thermocouple directly to the surface with the double sided tape, circumventing the use of the steel shim tab. Rather than painting the outer surface of the thermocouple and the expose double sided tape, black electrical tape was placed over each thermocouple after it had been attached with double sided tape. The results of this method are shown in Figure 2.21. This method still suffered from the same flaws as the previous method in that the thermocouple region was still a noticeable cooler temperature (darker) than the surrounding areas, and the flow effects were still somewhat noticeable. However, the black electrical tape did become "invisible" further away from the "bump" of the surface thermocouple underneath. This suggested that the temperature under the tape was not influenced by the presence of the tape. This was confirmed by placing a piece of clear scotch tape over a thermocouple and viewing it with an IR camera, shown in Figure 2.23. This image suggested that the dark spot was simply a result of the optical properties of the tape.
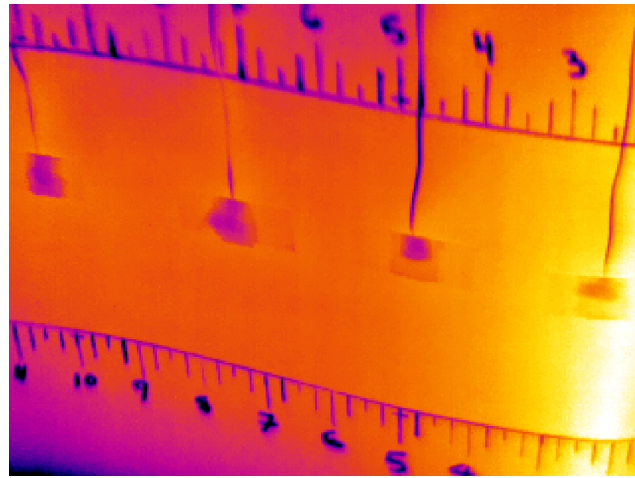
Figure 2.21: Black Electrical Tape Method

In order to overcome the optical properties of the black electrical tape, surface measurements of the IR camera were made just below the thermocouple on the IR image, as shown in Figure 2.22. This was due to a distortion of the image in the area immediately on and around the thermocouple location. Just below the thermocouple, the surface temperature measurements were assumed to be the same as just beneath the thermocouple, as the flow was 2-dimensional (set by the pressure distribution).
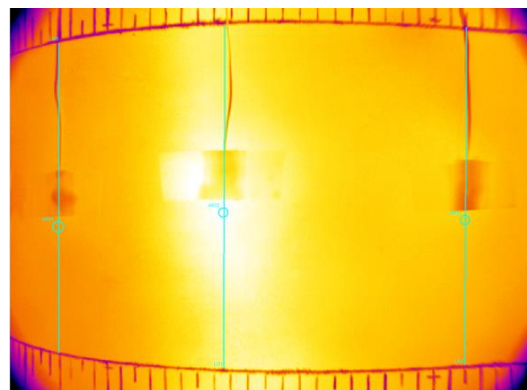
Figure 2.22: Example of Surface IR Temperature Measurements

The surface IR temperatures were then plotted against the corresponding thermocouple surface measurements to generate a calibration plot. This process was completed multiple times in separate experiments to determine the test-to-test repeatability of the calibration, with the goal of establishing a single calibration that could be used for every experiment. To do so, the calibration of each thermocouple for each camera was averaged together to produce a single calibration curve for each combination. An example of the results for two thermocouple and IR camera combinations are shown in Figure 2.24.
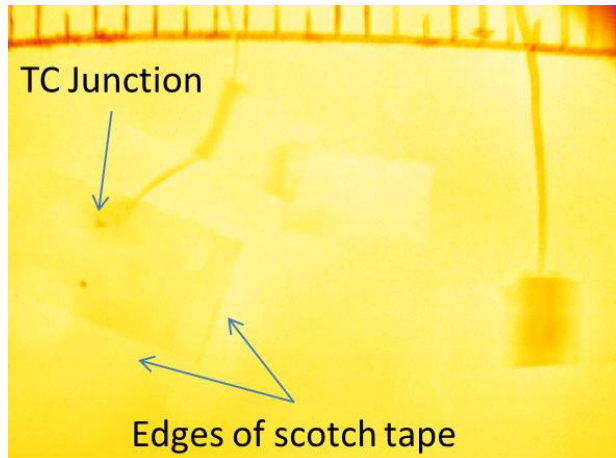
Figure 2.23: Clear Scotch Tape Example

During the calibration process, it was observed that due to the steep viewing angle of several camera positions that there was sensitivity to spatial locations. That is, along the curvature of the airfoil, the measured IR temperature would vary due to the change in effective viewing angle of the camera. Figure 2.25 and Figure 2.26 show the locations and corresponding calibration curves for one of the IR cameras used during the test. It can be seen that the more extreme viewing angle of the camera, location 3, has a higher

calibration curve, while the most normal viewing angle, location 5, has the lowest calibration curve.
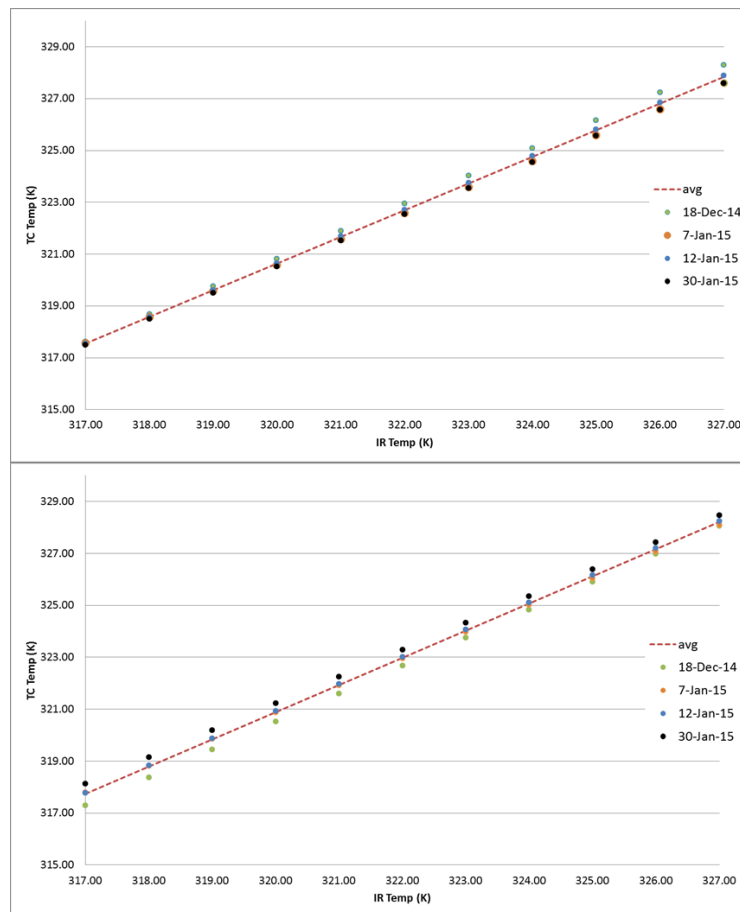
Figure 2.24: Example of Calibration Curves for two Camera-TC Combos
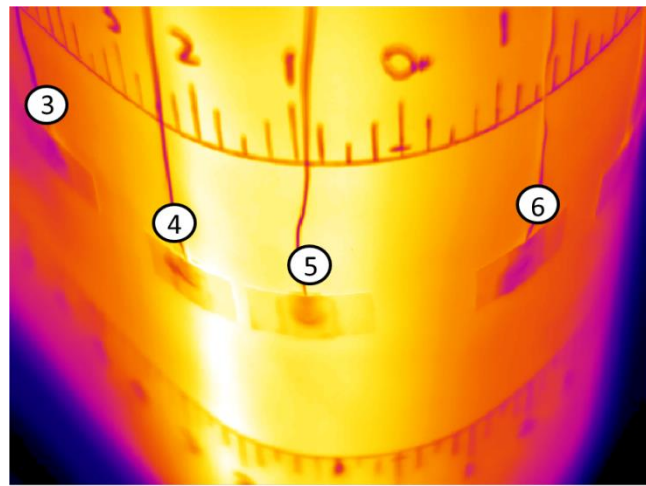
Figure 2.25: Locations of Thermocouples for Calibration
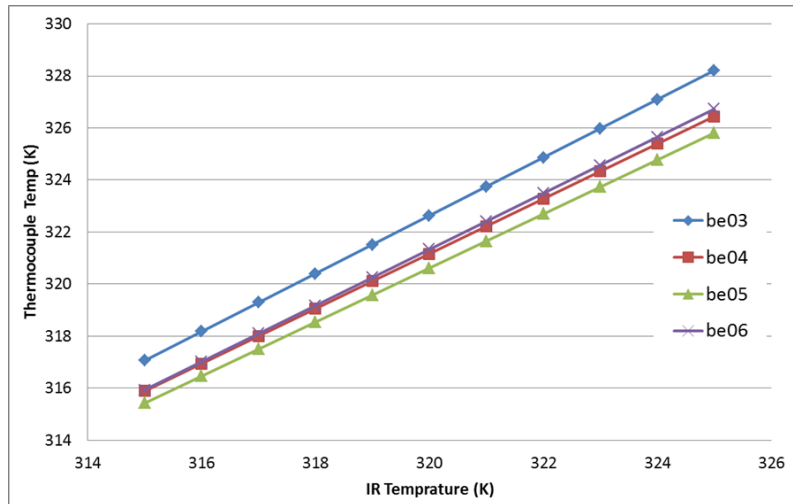
Figure 2.26: Calibration Curves corresponding to Figure 2.25

The interpolation used was a piecewise cubic interpolation (pchip interpolation in MATLAB). This interpolation scheme was used as it is shape preserving and offered a calibration that was smooth and tended to follow the variations in viewing angle from thermocouple to camera, as opposed to a linear interpolation or other non-linear

57

interpolation options, such as spline. It was for this reason that the "pchip" interpolation was used for both the IR camera calibration, and the internal thermocouple temperature maps. This difference in interpolations is illustrated in Figure 2.27. The location on the airfoil surface that this example was made is illustrated in Figure 2.28 for reference.
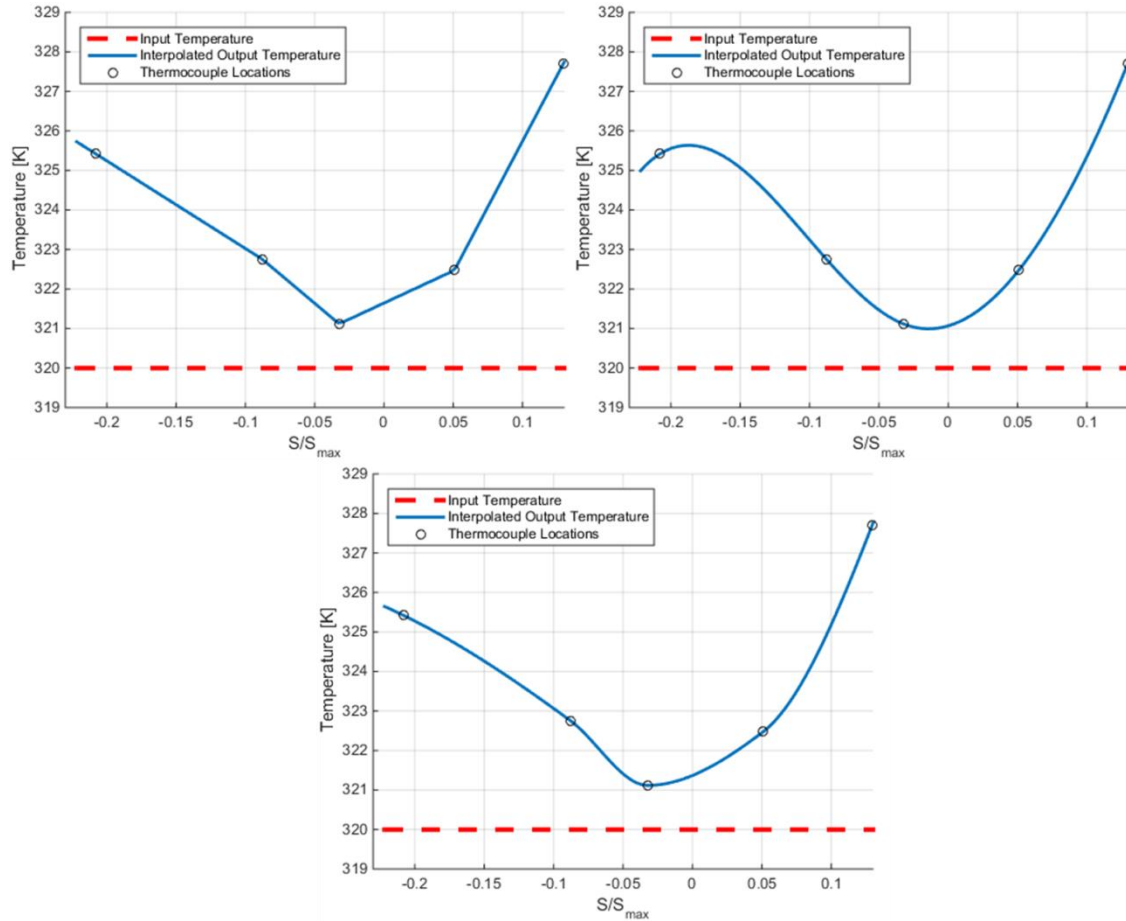
Figure 2.27: Interpolation Comparison: Linear (left) to Spline (right) and PCHIP (Bottom)

The interpolation process generated a calibration curve for each S/S_{max} position resulting in a smooth transition from one thermocouple location to another without

requiring a continuous calibration across the surface. This was particularly important for the thermocouples that were viewed by two different cameras. Prior to the interpolation process being implemented, there were discontinuities in the temperature maps at the "seams," where the view changed from one camera to the next.
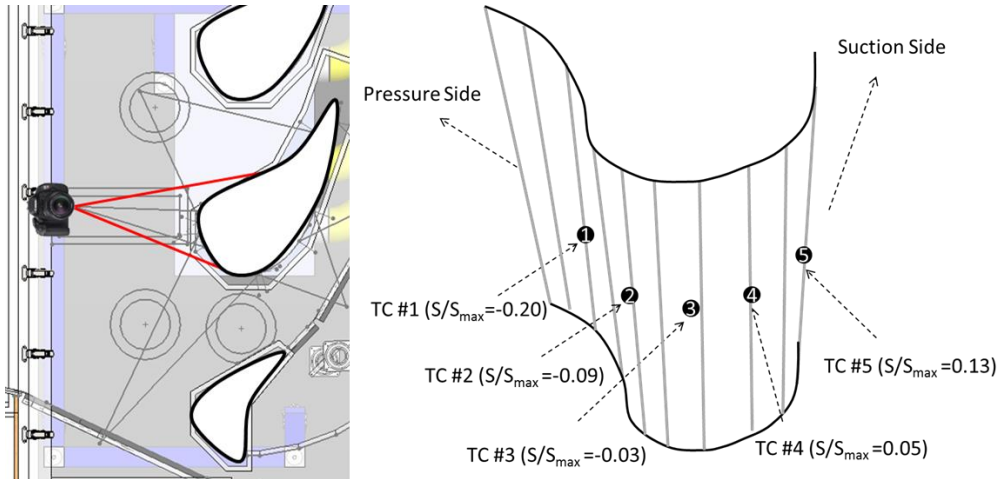
Figure 2.28: Reference of Airfoil Surface for Interpolation Example

2.6.7. Uncertainty in Heat Transfer Coefficient Measurements

Uncertainty in the IR camera calibrations was more complex than the uncertainty for the pressure transducers. While there was still a fossilized uncertainty in the standard, in this case the surface thermocouple imaged by the IR cameras, this was not the only source of uncertainty. An averaging process of several calibrations was used to generate a single calibration. In order to determine the uncertainty in this average calibration, the following equation was used.

Equation 2.16: $$\delta T_{IR} = \frac{2 * \sigma_{deviation}}{\sqrt{n}}$$

Equation 2.16 calculates the uncertainty of the temperature in the IR measurement due the use of an average of the calibration curves. Each camera-thermocouple combination generated a plot, such as the one shown in Figure 2.24, which consisted of several calibration curves and an average curve. Once this was done, an average deviation of each calibration curve from the averaged calibration was calculated by taking a difference of a given calibration curve from the corresponding average calibration curve at 10-12 set points. This average was then taken from each camera-thermocouple calibration, of which there were 16 total combinations, and used to generate a standard deviation, $\sigma_{deviation}$. This was the input used in Equation 2.16 to determine the uncertainty for each camera-thermocouple combination's calibration. The number of calibrations used to generate the average calibration for each camera-thermocouple combination, n, varied depending on the number of independent calibrations run for each combination, but was either $n = 3$ or $n = 4$. It should be noted that this was deemed an acceptable measure of the uncertainty due to averaging as the scatter in the calibration plots appeared to be random, i.e. there was no consistent trend of the calibration from one test relative to others.

Once this uncertainty effect on the IR temperature was calculated, it was combined with the fossilized uncertainty in the surface thermocouple calibration used for the IR calibration using a root-sum-square method. This combined uncertainty in the surface temperature was then propagated through Equation 2.15 to determine the contribution to the uncertainty in h.

In addition to IR calibration uncertainty, there was a bias uncertainty associated with the surface temperature images collected during the experimental measurements. These images of the heat flux plate showed a periodic variation in the temperature along

the radial direction, something unexpected due to the nominally 2-dimensional flow in the test section, which should have resulted in a uniform heat transfer coefficient in the spanwise direction of the airfoil. Examples of this variation are detailed in the results chapter.

To account for the periodic variation observed in the spanwise direction, at a given S/S_{max} location (stream-wise location along the curvature from the geometric leading edge non-dimensionalized by the curve length of the suction side of the Test Article), the standard deviation of the average heat transfer coefficient was determined. The average heat transfer coefficient was determined by averaging the 2-dimensional heat transfer map in the spanwise direction, resulting in a single heat transfer coefficient for each S/S_{max} location, also known as the laterally averaged heat transfer coefficient. Refer back to Figure 2.3 for a definition of curve length.

Equation 2.17:
$$\delta h = \frac{2\sigma_h}{\sqrt{n_{periods}}}$$

Using the standard deviation in the laterally averaged heat transfer coefficient, and the observed number of periods in the temperature variation, Equation 2.17 was used to estimate the magnitude of uncertainty in the measurement. This uncertainty was combined with the other uncertainties due to the propagation of all other measured values using a root-sum-square method. Table 2.4 lists the bias uncertainty for a selected heat transfer coefficient measurement. Note that the lateral variation was most significant on only one test condition, which is discussed in detail in the results chapter. The analysis performed for Table 2.4 used a representative value of the typical measurements, not the worst case.

All of the uncertainty presented was a bias that equally affects any of the heat transfer measurements made. It is important to recognize that the precision uncertainty then becomes the defining factor for comparing the heat transfer coefficient data between tested cases. To quantify the precision uncertainty, repeat tests were performed for two of the cases. These repeat cases showed an uncertainty $\delta h = \pm 2\, W/m^2 \cdot K$. This was determined by considering the average difference between the data sets. An example plot of the 35° test data and repeat test data shows the test to test repeatability data that was used to determine this uncertainty is shown in Figure 2.29.

Table 2.4: Example of Bias Uncertainty in HTC Measurements

Source of Uncertainty	Magnitude of Uncertainty	Units	% Effect on HTC
Temperature Average (Mainstream)	0.5	K	2.4
IR Calibration	0.36	K	1.8
Lateral Variations in IR Data	0.47	W/m^2-K	1.5
Radiation Heat Flux	4.1	W/m^2	0.6
Heat Flux Measurement	3.8	W/m^2	0.6
Heat Flux Foil Area	1.3×10^{-3}	m^2	0.4
Conduction Heat Flux	1.06	W/m^2	0.2
Total Uncertainty	**1.11**	**W/m^2-K**	**3.5**
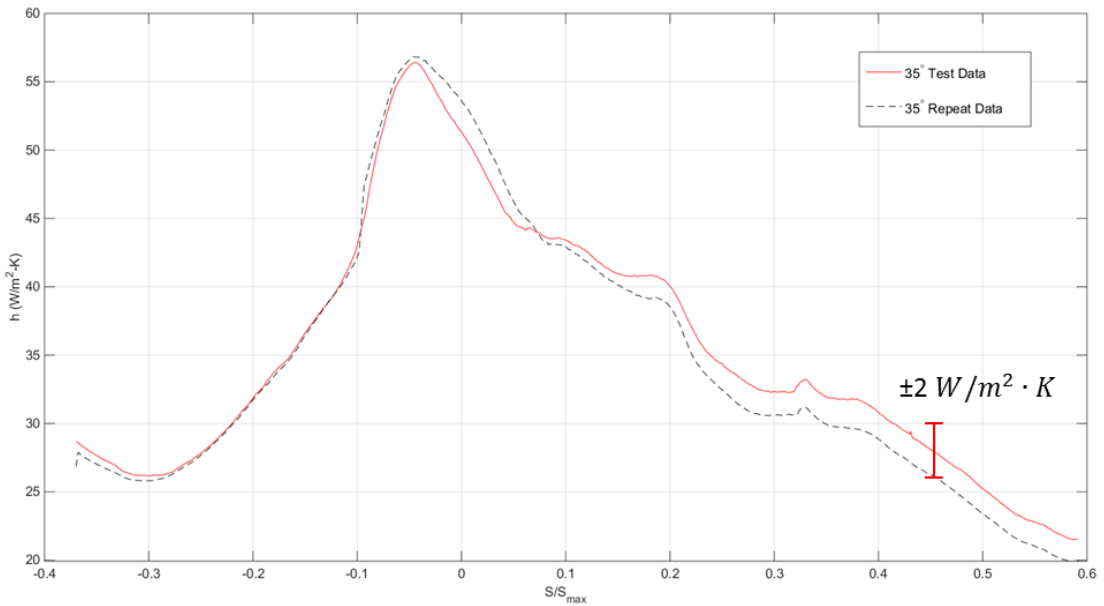
Figure 2.29: Example of Test to Test Repeatibility of HTC Measurements

2.7. TEST ARTICLE C

As briefly mentioned in the introduction of this thesis, one method of preventing damage to a turbine airfoil by the hot gas temperatures entering the turbine section is film cooling. This section covers the design and manufacture of a film cooling test article. It does not cover any experimental setups or measurements utilizing the model as those were beyond the scope of the work contained within this thesis.

2.7.1. Purpose

The goal for Test Article C was to collect data on the adiabatic effectiveness of the airfoil design under test. Adiabatic effectiveness is a design metric used heavily by industry when designing film cooling configurations. Details on the use and collection of adiabatic effectiveness can be found in literature, specifically Bogard and Thole [13].

63

2.7.2. Design and Manufacture

Adiabatic effectiveness requires the material of the airfoil to feature a relatively low thermal conductivity. For this reason, the airfoil was once again made out of the R-3315 "Last-A-Foam." The difficulty with designing and building Test Article C was the inclusion of film cooling holes on various areas of the external surface, as well as internal channels with rib turbulators to feed coolant to the film cooling holes.

To facilitate the build-up, the Test Article was once again built out of profile slices 3" thick, just as Test Article's A&B. However, the primary difference here was the presence of hatches. The hatches, illustrated in Figure 2.30, were cut outs of the airfoil surface where the film cooling holes were located to facilitate their machining, as well as introduce modularity to the Test Article should there be a desire to try different film cooling configurations in the future. Thus, the Test Article was split into a core model, 3 hatches, and 6 rib turbulators.

The hatches were constructed out of the same material as the core model, also out of 3" thick profile slices. They were made to be 18" long, to facilitate the use of 3" thick foam blocks. Once the profiles were cut, they were glued by hand using fast dry Gorilla Glue.
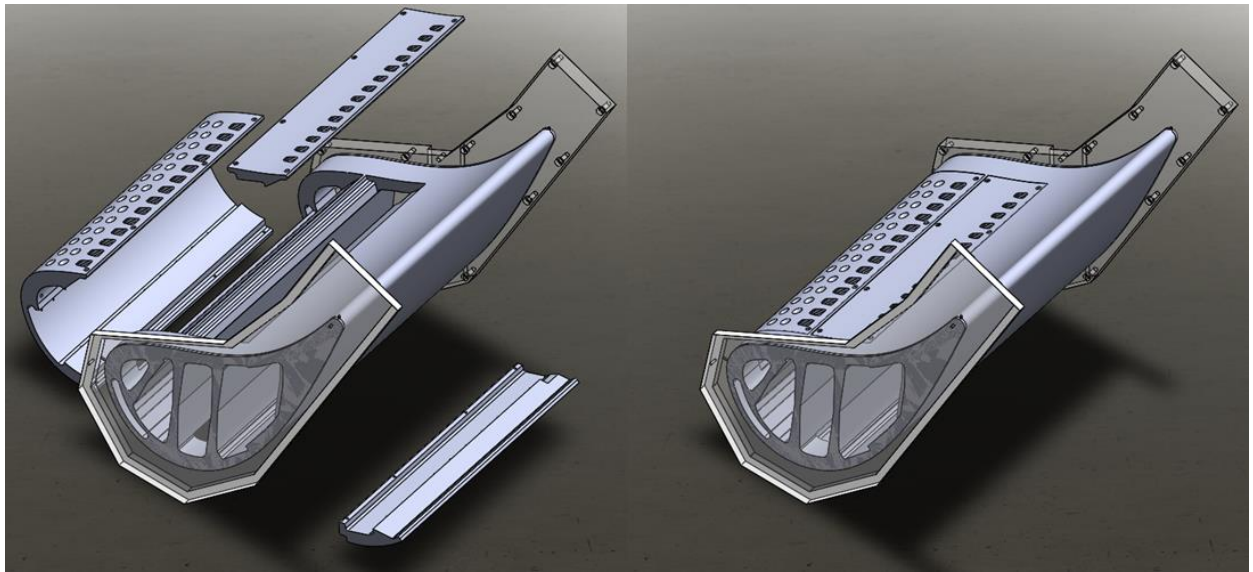
Figure 2.30: Exploded View (left) and Hatches Attached (right)

In addition to the hatches, there were rib turbulators that lined the outside edges of the channels within the Test Article. For Test Article C, these turbulators were made out of 6/6 Nylon, a design choice made to increase the structural integrity of the turbulators, as they were long, thin strips with small (0.10") chevron shaped ribs along the length, shown in Figure 2.31.

Prior to machining the film cooling holes on the hatches, the trip strips were glued to the pre-designed slot of each hatch, also using fast dry Gorilla Glue. The machining of the film cooling holes for the smaller hatches was outsourced to a local machine shop, Reed Prototype & Machining. Most of the film cooling holes to be machined were located on the leading edge hatch, and were done in-house in the M.E. Department machine shop. The impingement holes of the core model were also completed in-house after the core model had been glued together.

Figure 2.31: Rib Turbulators, Nylon (left) and Corian (right)

Once all the film cooling holes were properly machined and all turbulators had been glued into place, the hatches were attached to the core model. This was accomplished by having mounting holes machined along the lengths of the hatches. The hatches were then placed into position on the core model, and the hole locations were marked. The hatches were removed and the holes on the core model were drilled out to allow for the placement of a 3/8" 6/6 nylon spacer with a #6 size brass helicoil insert (9/32" in length) to be glued into position. These helicoil inserts were embedded at each location there was a mounting hole for the hatch using epoxy. It should be noted that a 0.03" gap was left around the perimeter, and the depth of the flanges, of the hatch and the core model where it was attached to allow for the placement of weather-stripping. Additionally, a general fitting tolerance of 0.01" was used for the rib turbulators to account for machining tolerances.

After the hatches were mounted, thermocouples and static pressure taps were epoxied to the internal channels of the model. The pressure taps were designed and SLS printed by the Sponsor to fit the curvature of the Test Article's internal ribs to facilitate attachment. The same 0.05" hypodermic tubing used for Test Article A was used to

connect the pressure tap from the inside of the channels through the top acrylic lid. All thermocouples were epoxied into place and their wiring was also routed out the top lid with the pressure tap tubing. The holes used for routing were then closed off with a silicon caulk.

Once instrumentation was completed and the lids were both securely attached to the Test Article, it was painted matte black with silver paint pen fiducial marks to match Test Article B.

An inlet section was built into the bottom of the test section just below the location of the Test Articles. This airfoil inlet section served two purposes: to assist in supporting the airfoil model and to provide coolant to Test Article's C & D. The airfoil model attached to the airfoil inlet is shown in Figure 2.32.
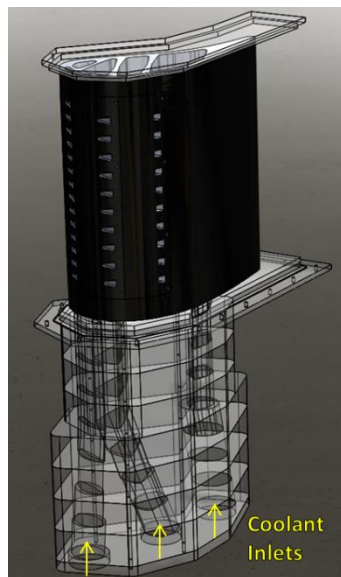

Figure 2.32: Airfoil Model Attached to Airfoil Inlet CAD Model

2.7.3. Improvements for Future Work

Test Article C was primarily a challenge to initially design. There were many features that had no precedence, such as overlapping hatches and internal rib turbulators. Short of gaining access to a 5-axis CNC, there are not many improvements that can be made to the process.

The overlapping hatch is something that may or may not be ideal. It was necessary due to the geometry of the airfoil and the requirement of the hatch to be securely attached to the core model. However, it led to issues with ensuring that there were no leaks from one hatch to the other, meaning the flow through the internal passages was only forced out of the film cooling holes, and not into another internal channel. In the end, this only required more liberal use of weather-stripping than originally conceptualized.

2.8. TEST ARTICLE D

Another method of preventing thermal wear to a turbine component is the use of internal cooling, often by necessity as the film cooling holes must be fed with coolant from the channels inside the turbine airfoils. In order to isolate the effects of the internal cooling and external film cooling, it is common to compare measurements between a model airfoil that has very low thermal conductivity with one that is more thermally conductive. This section details the design and manufacture of the latter to be used in future testing in conjunction with Test Article C, described in the previous section. Again, potential future testing is not outlined here as it is beyond the scope of this thesis.

2.8.1. Purpose

Test Article D was designed as a "conducting" model. The intent of Test Article D was to match the Biot number and the ratio of internal to external heat transfer coefficients during experimental testing to that of the engine conditions. This provides a model airfoil to measure the overall effectiveness, which takes into account the conduction of heat through the walls. Once again, this is a design metric that is of import to engine designers. More information on the importance of Biot matching and the use of overall effectiveness can also be found in literature by Dees et al. [14].

2.8.2. Design and Manufacture

The buildup of Test Article D was nearly identical to that of Test Article C with one primary difference, the material. As mentioned, the conductivity of the model was important. To achieve the correct thermal conductivity, the model was constructed out of DuPont's Corian ($k = 1\,W/m \cdot K$), a solid surface material used in kitchens and bathrooms across the nation.

The use of Corian had its challenges, the primary of which is that it is only ¾" thick. This resulted in a much larger number of pieces required to build the same size model as the other Test Articles. The first difficulty was getting the parts machined in a reasonable timeframe and within budget. To accomplish this, rather than machine them in-house, the parts were outsourced to Maximum Industries in Irving, Texas. There, the parts were machined on large routers, reducing estimated machine times from weeks to days.

It should be noted that the machining of Test Article C's profiles was also outsourced to Maximum at the same time to reduce difference between Test Articles. The

69

rib turbulators for Test Article D were also made of Corian, and were also machined by Reed Prototype & Machining at the same time as the nylon inserts for Test Article C.

Once all the pieces were in hand, the gluing began. DuPont's Corian Joint Adhesive was used to glue all the pieces together. The Test Article was then completed in the same fashion as described in Test Article C's buildup.

2.8.3. Improvements for Future Work

There was great difficulty in obtaining all of the Corian and joint adhesive used during the buildup. It is important for anyone attempting this in the future to make contact with the regional supplier. At the time of this writing, it was Artistic Counters. This can be verified by calling DuPont or the local Home Depot and inquiring about where the Corian comes from.

The other difficulty was obtaining ¾" thick Corian. This is manufactured in very small quantities and can therefore be difficult to locate. It is possible to use ½" Corian and have the sheets fused together by the supplier. Before going with the fused route, please discuss this option with the machinist that will be cutting the profiles to ensure there will be minimal to no tool deflection.

The most notable improvement that can be recommended is to add tabs to the individual parts. While this will increase the cost to machine, it is expected to greatly reduce the difficulty of building the core model itself. During the build of the current model, great care was taken to ensure that pieces were properly positioned using straight edged supports and weights, and yet the core model was still "crooked." The model was built up in sections, then each section was attached, and when the last section was to be placed, it did not align properly with the rest of the core model due to an ever so slight

variation in the gluing process of the other sections. There could have been many sources of the slight variations from glue thickness to machine tolerance. It is believed that tabs on the pieces would greatly improve the quality of the build and reduce the amount of sanding that was necessary to bring the current model into tolerance.

Outside of improvements to the current build process, if another material can be located that is more readily available and just as easily machinable that matches the required thermal conductivity, investigation is encouraged.

3. Results

This section details the results of the experimental measurements made for this thesis. The turbulence correlation results are discussed first, followed by the results of setting the pressure distribution for the heat transfer measurements and the results of the heat transfer coefficient measurements. Each topic will include discussion of the results.

3.1. TURBULENCE

The goal of the turbulence measurements was to validate the results previously measured by both Roach[11] and Mosberg[10], as discussed in section 1.3. It was shown that the results were similar to but did not match the work done by Mosberg for his thesis. However, the coefficient required to predict turbulence intensity at the leading edge of the linear cascade for this test section was verified, and the required turbulence intensity of 5% was met.

3.1.1. Turbulence Correlation

Hotwire measurements were conducted at a range of rig angles, beyond those used for heat transfer coefficient measurements, in order to empirically identify the correlation required to predict the turbulence intensity at the leading edge of any testable linear cascade configuration in the wind tunnel as discussed in section 1.3. The following correlation, based upon Roach[11] and Mosberg[10], was verified for the wind tunnel independent of the geometry of the test article used in the linear cascade:

Equation 3.1: $$Tu = A \left(\frac{x_f}{b} \right)^{-\frac{5}{7}}$$

Equation 3.1 shows the correlation which was verified. From the combined results of testing performed at $\beta > 35°$, $0°$, and $-25°$, shown in Figure 3.1, the measured coefficient was found to have a value of A= 0.75. This coefficient value differs from the previous results of both Roach and Mosberg ($A = 0.8$). One primary difference between the studies done by Roach and Mosberg and the measurements performed for this thesis was the presence of a linear cascade just downstream of the hotwire probe during the turbulence measurements. The presence of the linear cascade, as shown in Figure 2.2, had a very large effect on the velocity distribution as the probe was traversed across the test section, as shown in Figure 3.2.
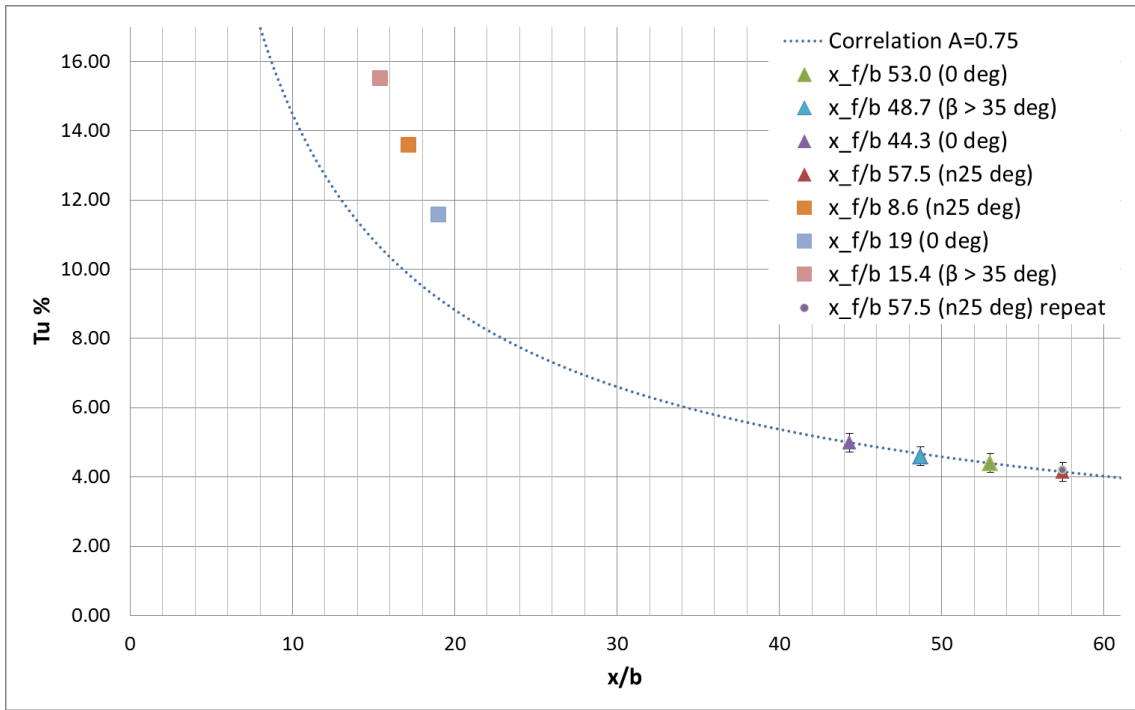
Figure 3.1: Turbulence Correlation and Measured Values

73
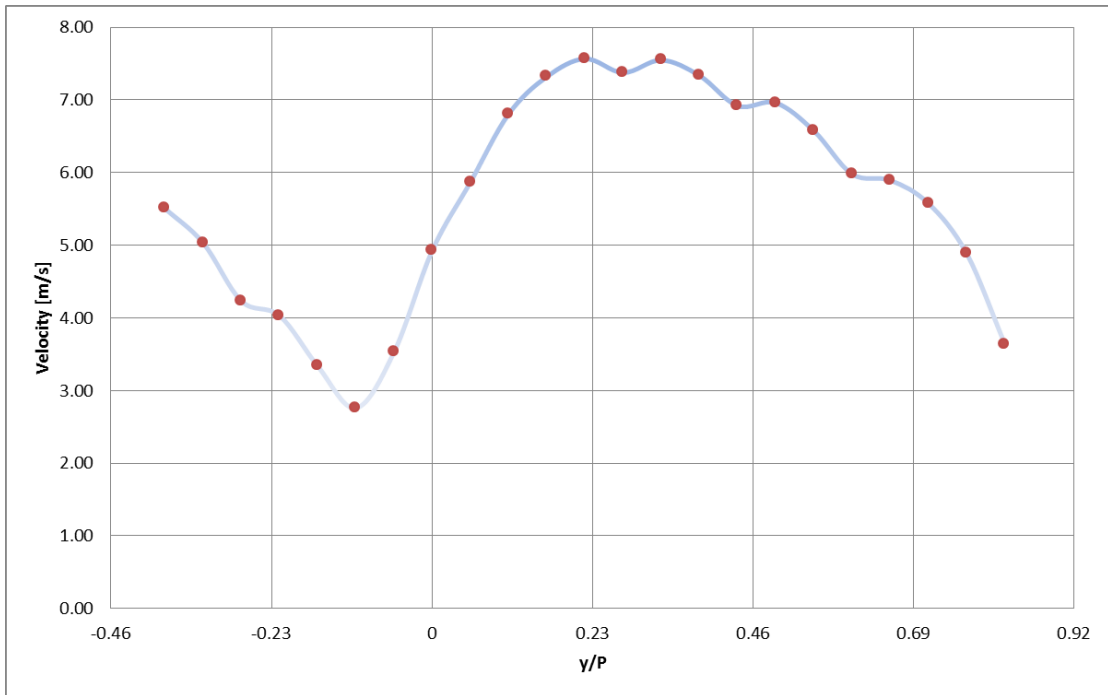
Figure 3.2: Example Velocity Profile (β~25°) taken 1" Upstream of Linear Cascade

As mentioned, the correlation value was measured at 3 different angles relative to the test section: $0°$, $-25°$ and $\beta > 35°$. Measurements were taken between the center Test Article and the 1/3 dummy airfoil in order to reach flow distances downstream of the grid that fell within the range of data provided by Mosberg. It was assumed that since the correlation held for both $0°$ and $\beta > 35°$ that any angle between the extremes would also work with the correlation. This, along with the application of symmetry down the centerline of the wind tunnel, was tested and confirmed with $-25°$.

Figure 3.1 shows the measured turbulence intensity for each angle versus the normalized flow distance at which it was measured. The correlation, plotted as a solid

line, passes within the uncertainty of each of the measured values made at the $44.3 < \frac{x_f}{b} < 57.5$ locations.

As mentioned in section 2.4.4, additional measurements were made much closer to the turbulence grid. These are also included in the plot for future reference. It is important to note that the correlation did not hold for these measurements that are much closer to the grid.

The data measured further downstream from the grid agrees with a correlation coefficient $A = 0.75$ for the tested flow distance (x_f / b) range from 44.3 to 57.5. This range was sufficient to allow for $5\% \, Tu$ to be generated at the leading edge plane of the linear cascade for all angles tested. It should be noted that Figure 3.1 has a verification point for the 0° case at $x_f/b = 44.3$. This data point was obtained by using the $A = 0.75$ correlation coefficient and determining the grid location necessary to generate $5\% \, Tu$ at the probe location which was then measured, thus further confirming the accuracy of the coefficient. A repeat test was performed for the $-25°$ configuration at $x_f/b = 57.5$ and is also shown on Figure 3.1 to provide a measure of the test to test repeatability.

It should be noted that the average turbulence value was determined by averaging the turbulence intensity measured in the passage between the Test Article and the 1/3 dummy airfoil, shown in Figure 3.3. Note that $z/P = 0$ corresponds to the leading edge of the center Test Article in the linear cascade, as defined in Figure 2.6.

One important reminder is that the measurements were made 1" upstream of the leading edge of the linear cascade in the passage between the blades. As such, these measurements were not verified by direct measurement at the leading edge of the test article. This was done specifically due to the large influence the blade has on the flow around the stagnation region.

75

It was recognized that the peak turbulence intensity occurred just upstream of the stagnation region on the airfoil's pressure side surface due to the presence of the airfoil influencing the flow. This was shown by Radomsky and Thole [15], noting that due to the difference in airfoil geometry, they measured a peak on the suction surface due to a different geometric leading edge location.

Furthermore, measurements were made of the freestream turbulence intensity without the turbulence grid. These measurements showed a uniform turbulence intensity of 0.6% between the turning vane wakes.

During the turbulence intensity measurements, data was also collected to determine the integral length scale. These measurements were approximately 6% $\pm$ 2% of the axial chord length of the airfoil. Additionally, refer back to Figure 2.6 for a schematic of the turbulence testing setup.
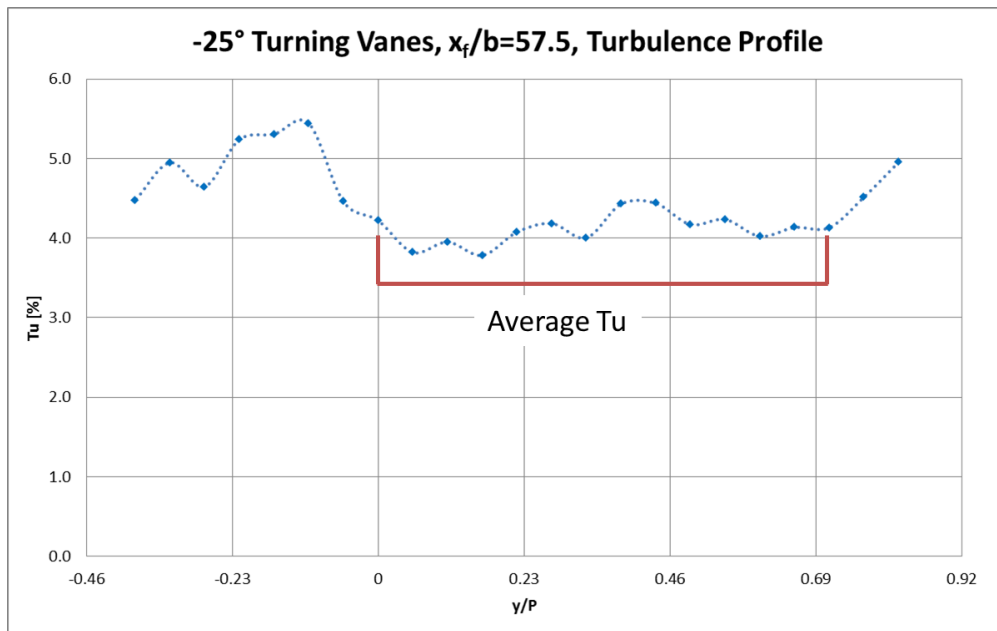

Figure 3.3: Example of Location for Averaged Turbulence Intensity

76

3.1.2. Flow Effects due to Turbulence Grid

During validation of the designed turbulence grids, it was discovered that the presence of the grid in the test section affected the angle of the inlet flow to the test cascade. This possibility was suggested by Mosberg during his design of the grids that were used; however, it was not until testing began in the new test section that the effect could be measured. Table 3.1 summarizes the testing conditions for each of the four cases experimentally tested. The incidence angles were measured by Kyle Chavez using a PIV system, as mentioned in section 2.3.1. For each test condition, the computationally predicted pressure distribution had inlet conditions adjusted to match the experimentally measured inlet angles.

Table 3.1: Testing Conditions

Case	Rig Inlet Angle	Engine Inlet Angle	Turbulence	Inlet Re_C
-35° High Tu	-30.1°	0.1°	5.0%	120,000
-25° High Tu	-21.2°	-8.8°	5.0%	120,000
-35° Low Tu	-33.7°	3.7°	0.6%	120,000
-25° Low Tu	-25.0°	-5.0°	0.6%	120,000

3.2. HEAT TRANSFER COEFFICIENTS

The primary goal of the experimental setup was to make measurements of the external heat transfer coefficient. This section provides the results of setting the pressure distribution to the CFD predicted levels to provide the expected flow conditions around the airfoil. It then details the results of the heat transfer coefficient measurements and compares the results to those found in literature.

77

3.2.1. Pressure Distribution

Prior to measuring heat transfer coefficients, the pressure distribution was set along the airfoil surface, as outlined in section 2.5.4. A sample plot of one such pressure distribution result is shown in Figure 3.4.
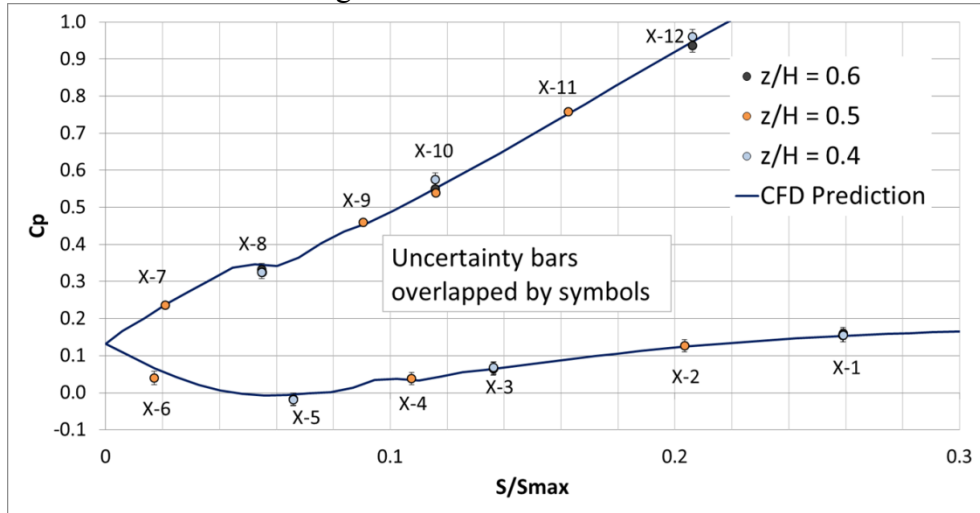
Figure 3.4: Example of Pressure Matching Measurements ($\beta \sim 35°$)

Coefficients of pressure were matched to the computationally predicted values very well, with only small deviations measured ($\Delta C_p \leq 0.02$). The spanwise (z/H) pressure measurements (x-1, 3, 5, 8, 10, & 12) were also matched to the predicted values at each of the tested spanwise locations ($z/H = 0.4, z/H = 0.5, z/H = 0.6$), with most of the measurements resulting in overlapping data points, indicating the measurements were very repeatable as expected since the test section was designed to produce a 2-dimensional flow. The x-10 and x-12 radial positions did show some variations in measurements, which were almost within uncertainty. Overall the 18 radial pressure measurements defined a nominally 2-dimensional flow and the 22 mid-span

pressure measurements verified a close match to the computationally predicted aerodynamic condition necessary to replicate the periodic boundary condition.

3.2.2. Heat Transfer Coefficients

Once the pressure distribution was set for a given angle, the heat transfer coefficient data measurements were made. As outlined previously, the heat transfer coefficients were measured as 2-dimensional images which were "flattened" and "stitched" together using a MATLAB script. The resulting contour plots are shown in Figure 3.5.

The contour plots showed a uniform heat transfer coefficient distribution in the spanwise direction, which was expected given that the flow was designed to be nominally 2-dimensional. However, the $-25°$ low turbulence case, showed a moderate variation in the spanwise direction. This variation was attributed to a flow field anomaly, likely caused by the turning vanes. This explanation was supported by the $-25°$ high turbulence case which did not show the same variation, suggesting that the flow field anomaly was upstream of the turbulence grid and was destroyed by its presence. In an attempt to further isolate the cause of the non-uniformity, the wind tunnel's mainstream velocity was reduced significantly and the heat flux plate was allowed to reach a steady condition. This process greatly reduced the non-uniformity of the surface temperatures seen on the IR cameras, suggesting that the flow field was the cause of the non-uniformity.

The contour plots also show red dashed lines that mark the location of the stagnation line for each tested case. It should be noted that the geometric leading edge is denoted as the 0 location on the plots, but the stagnation line is offset pressure side $(S < 0)$. As mentioned in section 2.5.4, the outer walls and bypass blockages were

adjusted to set the pressure distribution for the test article in the linear cascade. In addition to this, the stagnation lines, also a result of CFD predictions, was forced to a specific location. The uncertainty in setting these stagnation lines was much smaller $(\delta(\frac{S}{S_{max}}) < 1\%)$ than the variation listed. The peak heat transfer coefficient was found to be near to the stagnation lines but shifted toward the suction side. These values are listed in Table 3.2.
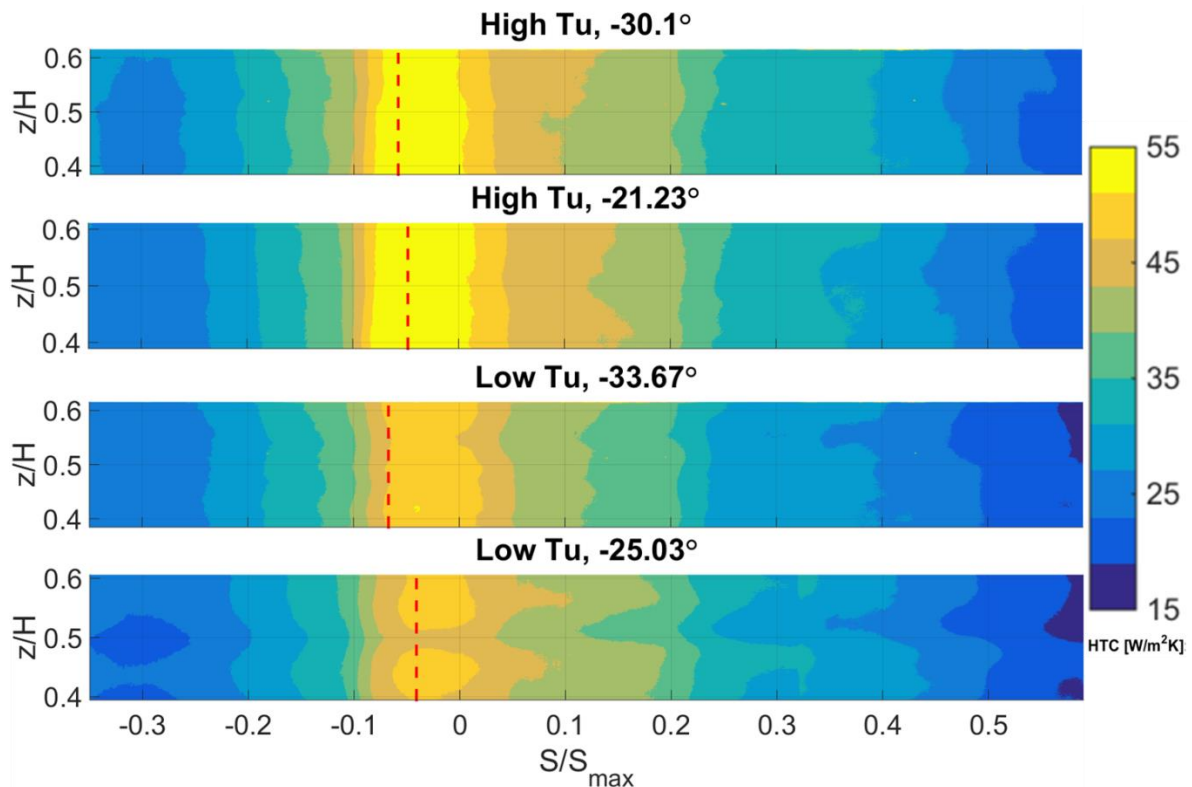

Figure 3.5: Heat Transfer Coefficients Contour Plots

The data from the contour plots was then averaged in the spanwise direction to produce laterally averaged plots, shown in Figure 3.6. These plots also show stagnation

lines for each of the tested cases. The shift between stagnation line, peak heat transfer coefficient, and geometric leading edge is more apparent in these plots.

Table 3.2: Peak h Location

Rig Inlet Angle	Engine Inlet Angle	Stagnation Line (S/S_{max})	Peak Laterally Averaged h Location (S/S_{max})
-30.10°	0.10°	-0.058	-0.044
-21.23°	-9.67°	-0.048	-0.046
-33.76°	3.76°	-0.067	-0.042
-25.03°	-4.97°	-0.041	-0.038

There was a nominally 10° shift in the incidence angle, within the precision uncertainty ($\delta h = \pm 2\ W/m^2 \cdot K$), yet there was no measureable effect associated with incidence angle. There was a measureable effect due to the mainstream turbulence level, with the higher turbulence cases having an $11 - 14\%$ increase in the heat transfer coefficients around the leading edge portion of the airfoil, and a 5% increase downstream on the pressure and suction surfaces.

An increase in the heat transfer coefficient due to an increased turbulence intensity has been previously documented by Carullo et al. [6]. As detailed in section 1.2.2, the largest heat transfer coefficient changes were measured by Carullo et al. at the transition regions on the pressure and suction sides of the airfoil. The measurements made for this thesis did not measure any such transition regions. However, range of airfoil pressure and suction surfaces that were measured showed a smaller effect of mainstream turbulence on h, ~5%, than the results shown in Carullo et al. where they showed an increase of ~25%. The stagnation region augmentation of h, 11-14%, was more comparable to 15-20% that Carullo et al. presented. However, the tests performed

by Carullo et al. were at a much higher freestream turbulence intensity of $12 - 14\% \, Tu$ compared to the $5\% \, Tu$ generated for the experimental measurements of this thesis.
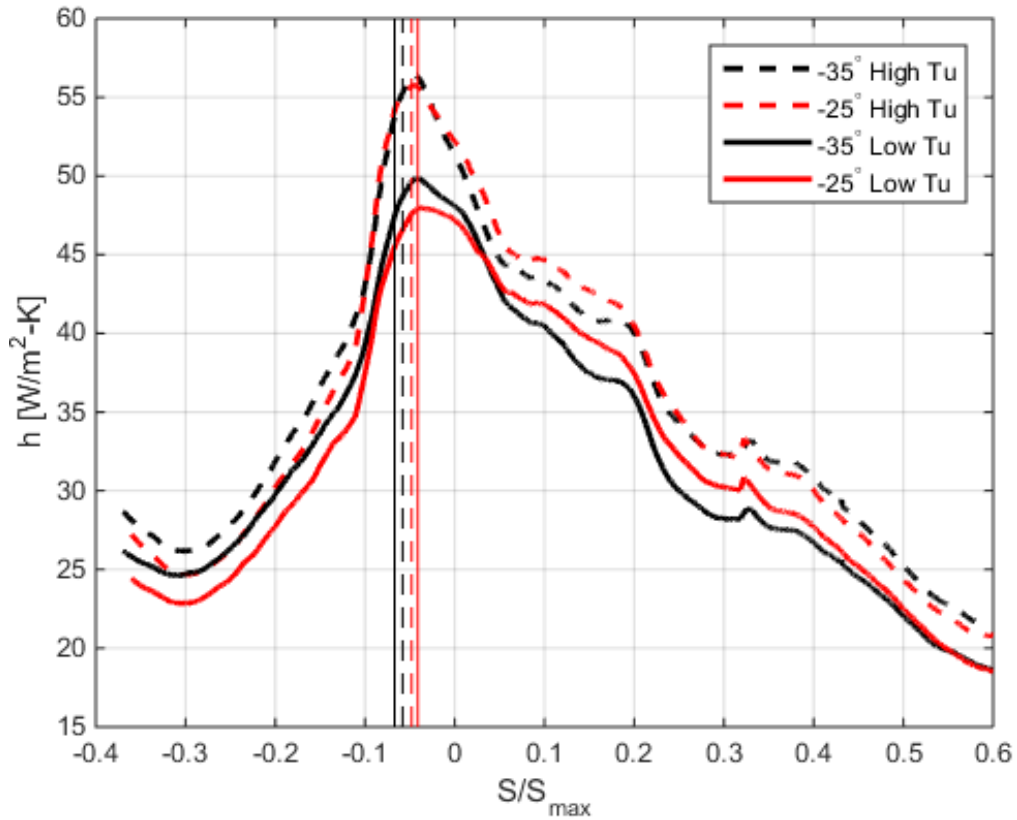
Figure 3.6: Laterally Averaged Heat Transfer Coefficient Distributions

Comparing the results of these measurements to the data presented by Consigny and Richards[7], there is a much closer agreement. Consigny and Richards generated a $0.8 - 5.2\% \, Tu$ just upstream of the linear cascade. This change in freestream turbulence intensity resulted in an augmentation of the external heat transfer coefficient at the leading edge region of ~15%. This is very similar to the $11 - 14\%$ augmentation shown in Figure 3.6. Furthermore, the pressure side augmentation levels tended to show smaller

influence of turbulence intensity, on the order of $5 - 10\%$ increases in h, which again was similar to the results measured here. Despite this, Consigny and Richards did show much larger variations on the suction side, ~200% increase in h, largely associated with the transition region. This was also apparent on the pressure side of some test cases they presented. These variations were not measured for this thesis as the transition regions were not present within the viewed surfaces.

Gandavarapu and Ames[16] validated an empirical correlation, one originally proposed by Ames in his PhD Dissertation, to predict the stagnation region heat transfer coefficient augmentation due to diameter of the leading edge, freestream turbulence intensity and lengthscale, and Reynolds number, as shown:

Equation 3.2: $$\frac{Nu}{Nu_0} = 1 + 0.04 * Tu \left(\frac{D}{\lambda_f}\right)^{\frac{1}{3}} Re_D^{\frac{5}{12}}$$

where D is the diameter of the leading edge region. Using Equation 3.2 with the large diameter of the leading edge for the airfoil tested, the heat transfer coefficient increase due to increased turbulence intensity was expected to be 30%.

However, the tests performed by Gandavarapu and Ames were conducted using a symmetrically flat object with a rounded leading, a very simplified geometry that is not necessarily representative of an airfoil. Furthermore, in the complex curvature of the tested airfoil model, it is uncertain as to where to define the effective diameter of the leading edge, which leads to a wide range of potential diameters. If one were to use the smaller range of the potential diameters, the prediction of the heat transfer coefficient augmentation due to freestream turbulence is much closer to the measured values(~15%). However, it is more likely that the diameter, based upon the stagnation

line for the tested angles, is on the larger end of the potential diameters, hence the 30% predicted rise in heat transfer coefficient. Overall it is unclear if this correlation is applicable to the airfoil geometry tested. Dees[8] also showed that the Equation 3.2 over predicted the leading edge heat transfer coefficient for the C3X Vane by $15 - 25\%$.

4. Conclusions and Future Work

4.1. CONCLUSIONS REGARDING THE WIND TUNNEL

The results of this thesis extend beyond the experimental data that was collected and presented in the results section. A milestone for the TTCRL was reached upon completion of the validation of the new test section that was designed and constructed to facilitate these experimental measurements.

Great lengths were taken to measure the overall functionality of the new test section. This required solving loss issues in one of the bypass loops and making numerous flow measurements to verify the incidence angle of each turning vane set in order to establish the correct flow conditions. Much of this work was accomplished with Kyle Chavez, a PhD Candidate also working on the project. He also devoted a great deal of his time to rewriting in house MATLAB scripts and LabVIEW programs to help facilitate all the future testing that might be accomplished with the new test section. An example of one such improvement to the programming includes the ability to match pressure distributions around a given airfoil geometry to the CFD prediction in real time, which proved an invaluable tool during initial configuring of the adjustable walls and blockages.

The turbulence experiments performed by Noah Mosberg that were validated for this thesis have become a standard for setting turbulence levels in the test section. The same process was done with the previous iteration of the test section which saved countless hours of work by establishing criteria that others could rely upon to achieve the boundary conditions required for a specific test setup.

85

4.2. FUTURE WORK REGARDING THE WIND TUNNEL

The new test section will be around for years to come, if the history of the TTCRL holds strong. Like all initial testing, there is plenty of room for improvements, room for finesse and patience where there was previously only a perpetually slipping schedule demanding more assumptions.

The best and most critical assumption that could be further explored is the turbulence correlation. The results of the experiments showed that the coefficient used in the turbulence correlation ($A = 0.75$) was not a function of turning angle, or at the least the functional dependence was very weak. This assumption is not critical, as the uncertainty in the coefficient had a negligible effect on the uncertainty in turbulence. However, if future testing requires a lower absolute measure of the correlation's uncertainty, or insurance against possible dependence on incidence angle, more testing would be required. It would be recommended to make attempts at measuring this using a PIV over the hot wire system. The calibration process for the hotwire was difficult due to the wakes of the turning vanes. These wakes seemed to introduce a velocity bias in the calibration. A PIV would not require such a calibration and would provide a higher resolution data set of the flow field. The PIV would also allow measurements much closer to the airfoil surface than the hotwire probe.

4.3. CONCLUSIONS REGARDING THE EXPERIMENTAL RESULTS

In general, the work done setting the boundary conditions (i.e. turbulence and pressure distribution) for the airfoil design tested went as planned. That is due mostly to the work that went into designing and verifying the new test section to function as expected. The pressure distributions were set without too much hassle using the real time

CFD prediction to measurement comparison plots. Turbulence levels were set using the correlation, and the heat transfer coefficient measurements followed.

The heat transfer coefficient results showed an rise in $11 - 14\%$ due to a freestream turbulence intensity increase of 0.6% to 5.0%, which tended to agree with results presented by Consigny and Richards[7], but only for test cases that did not exhibit large variations in transition regions. This is potentially due the design of the airfoil geometry tested for this thesis.

The uncertainty in the measurements presented was not large enough to account for the gap between the results of the measurements made for this thesis and those presented in literature, specifically in the showerhead region TRL predictions made by Gandavarapu and Ames[16]. Their prediction suggested that the augmentation to h should have been closer to 30% on the stagnation region, but measurement results showed only $11 - 14\%$.

Additionally, it was expected to see an effect of incidence angle, but due to the uncertainty, again no discernable effect could be shown. Giel et al. showed that the largest effect of incidence angle on h was a shifting of the transition location on the suction side of the airfoil, but that region was not within the measurement range of the IR cameras.

4.4. FUTURE WORK REGARDING THE EXPERIMENTAL RESULTS

As mentioned, the uncertainty in the h measurements resulted in no measureable effect with incidence angle. Future work could be performed in attempting to reduce this uncertainty such that it could be verified as to whether the airfoil geometry or the uncertainty was the cause. The difficulty in doing so lies in the calibration of the IR

87

cameras. The methods for improvements of such were already discussed in section 2.6.3 and will not be repeated.

Additional work could be performed to attempt to image further downstream in hopes of measuring a turbulent transition location on the suction side of the airfoil. Due to the limits on IR camera availability, this was not an option for this thesis.

References

[1]   Moran, M. J., and Shapiro, H. N., 1999, Fundamentals of Engineering Thermodynamics, John Wiley & Sons, New York.

[2]   "Wadley Research Group - UVA" [Online]. Available: http://www.virginia.edu/ms/research/wadley/high-temp.html. [Accessed: 09-Apr-2015].

[3]   Giel, P. W., Boyle, R. J., and Bunker, R. S., 2004, "Measurements and Predictions of Heat Transfer on Rotor Blades in a Transonic Turbine Cascade," J. Turbomach., **126**(January 2004), p. 110.

[4]   Camci, C., and Arts, T., 1991, "Effect of Incidence on Wall Heating Rates and Aerodynamics on a Film-Cooled Transonic Turbine Blade," J. Turbomach., **113**(90), p. 493.

[5]   Arts, T., Duboue, J.-M., and Rollin, G., 1998, "Aerothermal Performance Measurements and Analysis of a Two-Dimensional High Turning Rotor Blade," J. Turbomach., **120**(3), p. 494.

[6]   Carullo, J. S., Nasir, S., Cress, R. D., Ng, W. F., Thole, K. a., Zhang, L. J., and Moon, H. K., 2011, "The Effects of Freestream Turbulence, Turbulence Length Scale, and Exit Reynolds Number on Turbine Blade Heat Transfer in a Transonic Cascade," J. Turbomach., **133**(January 2011), p. 011030.

[7]   Consigny, H., and Richards, B. E., 1982, "Short Duration Measurements of Heat-Transfer Rate to a Gas Turbine Rotor Blade," J. Eng. Power, **104**(3), p. 542.

[8]   Dees, J. E., 2010, "Experimental Measurements of Conjugate Heat Transfer on a Scaled- up Gas Turbine Airfoil with Realistic Cooling Configuration."

[9]   Ames, F. E., 2015, "The Influence of Large-Scale High-Intensity Turbulence on Vane Heat Transfer," **1**(January 1997).

[10]   Mosberg, N., 2013, "Experimental Investigation of the Performance of a Fully Cooled Gas Turbine Vane with and without Mainstream Flow and Experimental Analysis Supporting the Redesign of a Wind Tunnel Test Section," MS Thesis, UT Austin, pp. 79–107.

[11]   Roach, P., 1987, "The generation of nearly isotropic turbulence by means of grids," Int. J. Heat Fluid Flow, **8**(2), pp. 82–92.

[12]   Moffat, R. J., 1988, "Describing the uncertainties in experimental results," Exp. Therm. Fluid Sci., **1**, pp. 3–17.

[13]   Bogard, D. G., and Thole, K. a., 2006, "Gas Turbine Film Cooling," J. Propuls. Power, **22**(2), pp. 249–270.

[14]   Dees, J. E., Bogard, D. G., Ledezma, G. a., Laskowski, G. M., and Tolpadi, A. K., 2009, "Experimental Measurements and Computational Predictions for an Internally Cooled Simulated Turbine Vane," Int. Mech. Eng. Congr. Expo.

[15]   Radomsky, R. W., and Thole, K. a., 2000, "Flowfield Measurements for a Highly Turbulent Flow in a Stator Vane Passage," J. Turbomach., **122**(2), p. 255.

[16]   Gandavarapu, P., and Ames, F. E., 2013, "The Influence of Leading Edge Diameter on Stagnation Region Heat Transfer Augmentation Including Effects of Turbulence Level, Scale, and Reynolds Number," J. Turbomach., **135**(1), p. 011008.

Vita

Gavin is a man of gentle birth spawned by sprawling suburb called Flour Bluff in Corpus Christi, Texas. After narrowly escaping the clutches of his high school overlords, he wandered the globe under the auspices of the United States Air Force. Years later, weary from travel, craving the humid heat and delicious ozone of home, he returned to Texas. It was not long before the longing of knowledge filled his curious spirit, and he took up the quest for a higher education. Little did he know, he was playing right into "Their" hand. Countless hours were poured into completing the quest, into acquiring the titles most recognized by the markets of the free world. Now his quest is complete, even the hidden bonus was fulfilled, and he was dubbed a Master of Science. The maw of capitalism salivates at the thought. But our intrepid hero swallows his uncertainty and puts one foot after another, following the trail of shining gold that litters the path. Somewhere, deep inside his mind, he remembers a dream of sharing his creativity and imagination with the world, but that couldn't be real. How could he survive on such a pittance?

gavin.r.packard@gmail.com

This thesis was typed by Gavin Ray Packard